

---

**1 Local Wind Regime Induced by Giant Linear Dunes:  
2 Comparison of ERA5-Land Reanalysis with Surface  
3 Measurements**

**4 Cyril Gadal · Pauline Delorme ·  
5 Clément Narteau · Giles F.S. Wiggs ·  
6 Matthew Baddock · Joanna M. Nield ·  
7 Philippe Claudin**

**8**  
**9 Received: DD Month YEAR / Accepted: DD Month YEAR**

**10 Abstract**

**11** Emergence and growth of sand dunes results from the dynamic interaction  
**12** between topography, wind flow and sediment transport. While feedbacks be-  
**13** tween these variables are well studied at the scale of a single and relatively  
**14** small dune, the average effect of a periodic large-scale dune pattern on at-  
**15** mospheric flows remains poorly constrained, due to a pressing lack of data  
**16** in major sand seas. Here, we compare local measurements of surface winds  
**17** to the predictions of the ERA5-Land climate reanalysis at four locations in  
**18** Namibia, both within and outside the giant linear dune field of the Namib  
**19** Sand Sea. In the desert plains to the north of the sand sea, observations and  
**20** predictions agree well. This is also the case in the interdune areas of the sand

---

C. Gadal

Institut de Mécanique des Fluides de Toulouse, Université de Toulouse Paul Sabatier, CNRS,  
Toulouse INP-ENSEEIHT, Toulouse, France. E-mail: cyril.gadal@imft.fr

P. Delorme

Energy and Environment Institute, University of Hull, Hull, UK.  
School of Geography and Environmental Science, University of Southampton, Southampton,  
UK.

C. Narteau

Université Paris Cité, Institut de physique du globe de Paris, CNRS, Paris, France

Giles F.S. Wiggs

School of Geography and the Environment, University of Oxford, Oxford, UK.

M.C. Baddock

Geography and Environment, Loughborough University, Loughborough, UK.

J.M. Nield

School of Geography and Environmental Science, University of Southampton, Southampton,  
UK.

P. Claudin

Physique et Mécanique des Milieux Hétérogènes, CNRS, ESPCI Paris, PSL Research Uni-  
versity, Université de Paris, Sorbonne Université, Paris, France.

21 sea during the day. During the night, however, an additional wind component  
22 aligned with the giant dune orientation is measured, in contrast to the easterly  
23 wind predicted by the ERA5-Land reanalysis. For the given dune orientation  
24 and measured wind regime, we link the observed wind deviation (over 50°) to  
25 the daily cycle of the turbulent atmospheric boundary layer. During the night,  
26 a shallow boundary layer induces a flow confinement above the giant dunes,  
27 resulting in large flow deviations, especially for the slower easterly winds. Dur-  
28 ing the day, the feedback of the giant dunes on the atmospheric flow is much  
29 weaker due to the thicker boundary layer and higher wind speeds. Finally, we  
30 propose that the confinement mechanism and the associated wind deflections  
31 induced by giant dunes could explain the development of smaller-scale sec-  
32 ondary dunes, which elongate obliquely in the interdune areas of the primary  
33 dune pattern.

34 **Keywords** Atmospheric boundary layer · Sand dunes · Flow over hills

---

**35 1 Introduction**

36 The description of turbulent flows over complex topography is relevant for  
37 a large variety of different environmental systems (Sherman 1978; Walmsley  
38 et al. 1982; Baines 1995; Wood 2000; Venditti et al. 2013; Finnigan et al.  
39 2020). For example, the flow over hills is of primary interest for wind power,  
40 meteorological and air pollution phenomena (Taylor et al. 1987). The proper-  
41 ties of these flows are also key to the understanding of geophysical phenom-  
42 ena, including the formation of wind-driven waves on the ocean surface (Sulli-  
43 van and McWilliams 2010), dissolution bedforms (Claudin et al. 2017; Guérin  
44 et al. 2020), or sedimentary ripples and dunes (Bagnold 1941; Charru et al.  
45 2013; Courrech du Pont 2015). Importantly, the troposphere presents a vertical  
46 structure, with a lower convective boundary layer, of typical kilometer-scale  
47 thickness, capped by a stably stratified region (Stull 1988). The largest topo-  
48 graphic obstacles, such as mountains, can therefore interact with this upper  
49 region and lead to internal wave generation or significant wind disturbances,  
50 such as lee-side downslope winds (Durran 1990).

51 Compared to hills and mountains, aeolian sand dunes offer idealized ele-  
52 vation profiles for the study of atmospheric turbulent flow over topographies,  
53 due to their smooth shape, free of canopies. Besides, dunes provide a rather  
54 wide range of scales, from decameters to kilometers, and very often come in  
55 a fairly regular pattern, which further simplifies the flow structure analysis.  
56 Past studies have highlighted two important topographic feedbacks on the  
57 wind flow close to the dune/hill surface. First is the effect on wind speed, with  
58 documented flow acceleration on upwind slopes (Weaver and Wiggs 2011) and  
59 deceleration on downwind slopes (Baddock et al. 2007), where the speed-up  
60 factor is essentially proportional to the obstacle aspect ratio (Jackson and Hunt  
61 1975). Under multidirectional wind regimes with frequent wind reversals, this  
62 speed-up effect induces large differences in the amplitude and orientation of  
63 the resultant sediment transport between flat sand beds and the dune crests  
64 (Zhang et al. 2014; Rozier et al. 2019; Gao et al. 2021). In addition, the po-  
65 sition of maximum velocity is typically shifted upwind of the obstacle crest  
66 (Jackson and Hunt 1975; Claudin et al. 2013). This behaviour has been the-  
67oretically predicted by means of asymptotic analysis of a neutrally stratified  
68 boundary-layer flow over an obstacle of vanishing aspect ratio (Jackson and  
69 Hunt 1975; Mason and Sykes 1979; Sykes 1980; Hunt et al. 1988; Belcher and  
70 Hunt 1998; Kroy et al. 2002). Experiments in flumes (Zilker et al. 1977; Zilker  
71 and Hanratty 1979; Frederick and Hanratty 1988; Poggi et al. 2007; Bristow  
72 et al. 2022), in wind tunnels (Gong and Ibbetson 1989; Finnigan et al. 1990;  
73 Gong et al. 1996) and in field conditions at all scales (Taylor and Teunissen  
74 1987; Claudin et al. 2013; Fernando et al. 2019; Lü et al. 2021), have also  
75 documented this effect. Interestingly, a similar behaviour exists for the pres-  
76 sure perturbation, but with a slight downwind shift for the pressure minimum  
77 (Claudin et al. 2021).

78 The second effect, much less studied, is the flow deflection that occurs when  
79 the incident wind direction is not perpendicular to the ridge crest. While pre-

dicted to be small (less than 10°) in the linear regime valid for shallow topography (Gadal et al. 2019), significant flow steering has been reported in the field on the downwind side of steep enough obstacles, such as well-developed sand dunes (Tsoar and Yaalon 1983; Sweet and Kocurek 1990; Walker and Nickling 2002; Smith et al. 2017) and in particular coastal foredunes (e.g. Hunter et al. 1983; Rasmussen 1989; Walker et al. 2006, 2009; Hesp et al. 2015; Walker et al. 2017; de Winter et al. 2020), mountain ranges (Kim et al. 2000; Lewis et al. 2008; Fernando et al. 2019), and valley topographies (Wiggs et al. 2002; Garvey et al. 2005).

Wind measurements over sand dunes have been mainly performed over small bedforms, typically a few meters high (corresponding to several tens of meters long) (e.g. Mulligan 1988; Hesp et al. 1989; Lancaster et al. 1996; McKenna Neuman et al. 1997; Sauermann et al. 2003; Andreotti et al. 2002; Walker and Nickling 2002; Weaver and Wiggs 2011). For practical reasons, fewer studies have performed similar measurements on giant dunes (Havholm and Kocurek 1988), with kilometer-scale wavelengths and heights of tens of meters. However, such large dunes provide a choice configuration for the study of turbulent flows over a complex topography. First, one expects larger wind disturbances for larger obstacles. Secondly, their large size can make them interact with the vertical structure of the atmosphere (Andreotti et al. 2009). Third, they usually form large patterns in sand seas and thus behave as rather clean periodic perturbations, in contrast with isolated dunes. Finally, because the morphodynamics of aeolian bedforms is strongly dependent on the local wind regime (Livingstone and Warren 2019), one can expect to see the consequences of windflow disturbance by large dunes on neighbouring small dunes (Brookfield 1977; Ewing et al. 2006). A similar effect is observed on the properties of impact ripple patterns due to the presence of dunes (Howard 1977; Hood et al. 2021).

Atmospheric flows have been much studied at the desert-scale with climate reanalyses based on global atmospheric models (Blumberg and Greeley 1996; Livingstone et al. 2010; Ashkenazy et al. 2012; Jolivet et al. 2021; Hu et al. 2021; Gunn et al. 2021), such as ERA-40, ERA-Interim or ERA5 (Uppala et al. 2005; Dee et al. 2011; Hersbach et al. 2020). However, the spatial resolution of these reanalyses (tens of kilometers) implies average quantities that do not resolve the smaller scales of interest, which range from individual dunes to small mountains (Livingstone et al. 2010). Recently, the release of ERA5-Land has partly resolved this limitation by providing up to 70 years of hourly wind predictions at a 9 km spatial resolution (Muñoz-Sabater et al. 2021). However, its validity remains to be studied, especially in remote desert areas where assimilation of measured data is very low.

In this work, we compare local wind speeds and directions measured by meteorological stations at four different locations inside and north of the giant linear dune field of the Namib sand sea to the regional predictions of the ERA5-Land climate reanalysis. Where the meteorological stations are surrounded by a relatively flat environment, we show that local measurements and regional predictions agree well. The agreement is also good in the interdune areas of

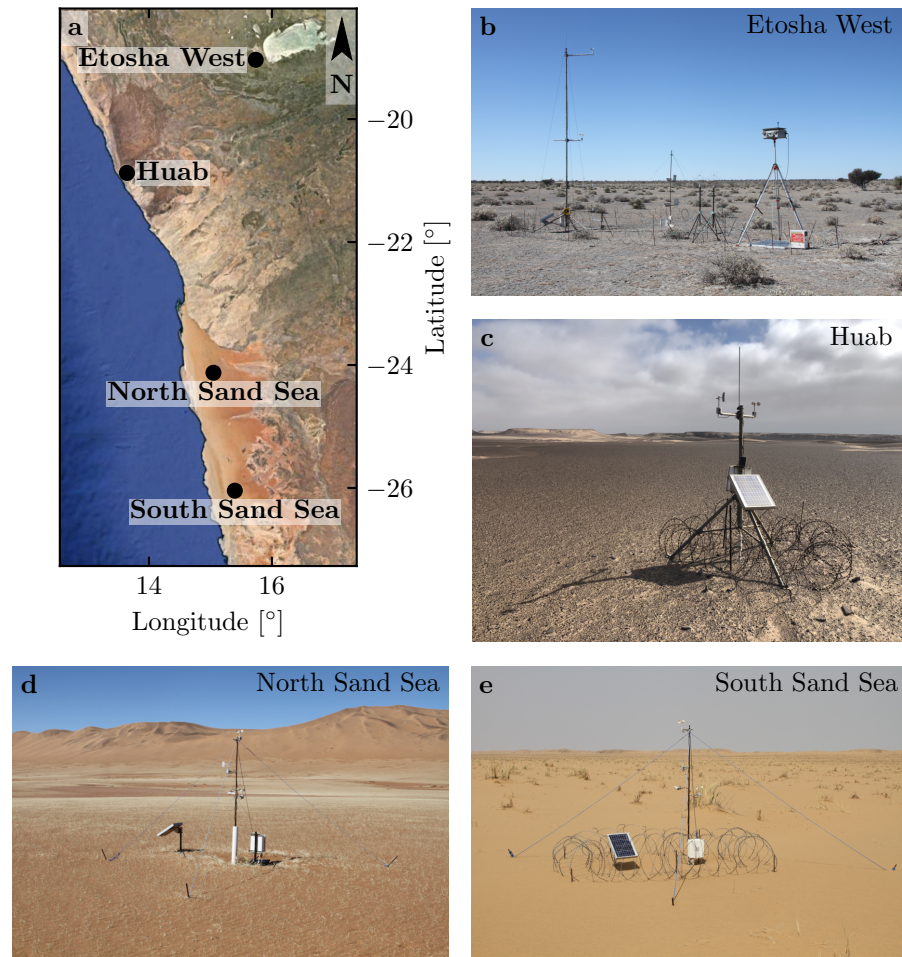


**Fig. 1** Studied field sites. **a** Location of the different sites in Namibia. **b-e**: Photographs of the meteorological stations.

the sand sea, except for some weak winds blowing at night, which exhibit an additional component aligned with the giant dune orientation. These winds are not predicted by the ERA5-Land reanalysis (Sect. 2). Further, we are able to link the magnitude of these differences to the circadian cycle of the atmospheric boundary layer (Sect. 3). Finally, we draw implications for the wind disturbances on smaller-scale dunes (Sect. 4), suggesting a possible origin for crossing dunes, a distinctive secondary dune form observed in the Namib and other sand seas.

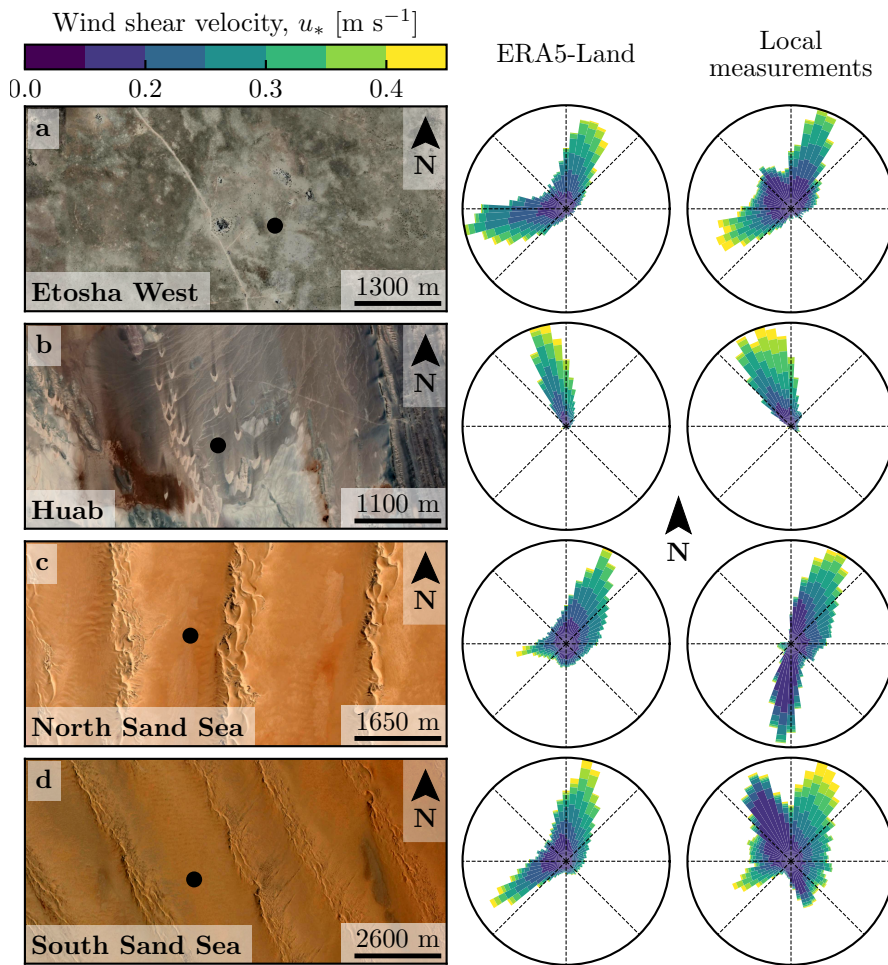


**Fig. 2** Wind data used in this study. Satellite images of the different environments (Google-Earth, Maxar Technologies, CNES/Airbus) are shown on the left. The black dots show the location of the wind measurements stations. On the right of the photos, the corresponding wind roses representing the data from the ERA5-Land climate reanalysis and the local wind stations are displayed. Note: the graphical convention for the wind roses is that the bars show the direction towards which the wind blows (see color bar for velocity scale).

## 134 2 Wind Regimes Across The Namib Sand Sea

135 We measured the wind regime at four different locations in Namibia, represen-  
 136 tative of various arid environments across the Namib desert (Figs. 1 and 2).  
 137 The Etosha West station was located at the Adamax waterhole to the west  
 138 of Etosha Pan in northern Namibia, in a sparsely vegetated area. The Huab  
 139 station was near the coast on a hyper-arid flat gravel plain lying north of  
 140 the ephemeral Huab river. Here, barchan dunes up to a few meters in height

141 develop from the sediment blowing out of the river valley (Nield et al. 2017;  
142 Hesp and Hastings 1998). These two stations were both located in relatively  
143 flat environments. In contrast, the North Sand Sea and South Sand Sea sta-  
144 tions were located in the interdunes between linear dunes with kilometer-scale  
145 wavelengths, hectometer-scale heights and superimposed patterns. In this sec-  
146 tion, we describe and compare winds from local measurements and climate  
147 reanalysis predictions.

## 148 2.1 Wind and Elevation Data

149 At each meteorological station (Fig. 1), wind speed and direction were sampled  
150 every 10 minutes using cup anemometers (Vector Instruments A100-LK) and  
151 wind vanes (Vector Instruments W200-P) at a single height, which was between  
152 2 m and 3 m depending on the station. The available period of measurements at  
153 each station ranged from 1 to 5 discontinuous years distributed between 2012  
154 and 2020 (Online Resource Fig. S1). We checked that at least one complete  
155 seasonal cycle was available for each station. Regional winds were extracted  
156 at the same locations and periods from the ERA5-Land dataset, which is a  
157 replay at a smaller spatial resolution of ERA5, the latest climate reanalysis  
158 from the ECMWF (Hersbach et al. 2020; Muñoz-Sabater et al. 2021). This  
159 dataset provided hourly predictions of the 10-m wind velocity and direction  
160 at a spatial resolution of  $0.1^\circ \times 0.1^\circ$  ( $\simeq 9$  km in Namibia).

161 To enable direct comparison, the local wind measurements were averaged  
162 into 1-hr bins centered on the temporal scale of the ERA5-Land estimates  
163 (Online Resource Fig. S2). As the wind velocities of both datasets were pro-  
164 vided at different heights, we converted them into shear velocities  $u_*$  (Online  
165 Resource section 1), characteristic of the turbulent wind profile. Wind roses  
166 in Fig. 2 show the resulting wind data.

167 Dune properties were computed using autocorrelation on the 30-m Digital  
168 Elevation Models (DEMs) of the shuttle radar topography mission (Farr et al.  
169 2007). For the North and South Sand Sea stations, we obtain, respectively,  
170 orientations of  $85^\circ$  and  $125^\circ$  with respect to the North, wavelengths of 2.6 km  
171 and 2.3 km and amplitudes (or half-heights) of 45 m and 20 m (Online Resource  
172 Fig. S4 for more details). This agrees with direct measurements made on site.

## 173 2.2 Comparison of Local and Regional Winds

174 The measured and predicted wind regimes are shown in Fig. 2. In the Namib,  
175 the regional wind patterns are essentially controlled by the sea breeze, result-  
176 ing in strong northward components (sometimes slightly deviated by the large  
177 scale topography) present in all regional wind roses (Lancaster 1985). These  
178 daytime winds are dominant during the period October–March (Fig. 3f and  
179 Online Resource Fig. 4f). During April–September, an additional (and often  
180 nocturnal) easterly component can also be recorded, induced by the combina-  
181 tion of katabatic winds forming in the mountains, and infrequent ‘berg’ winds,

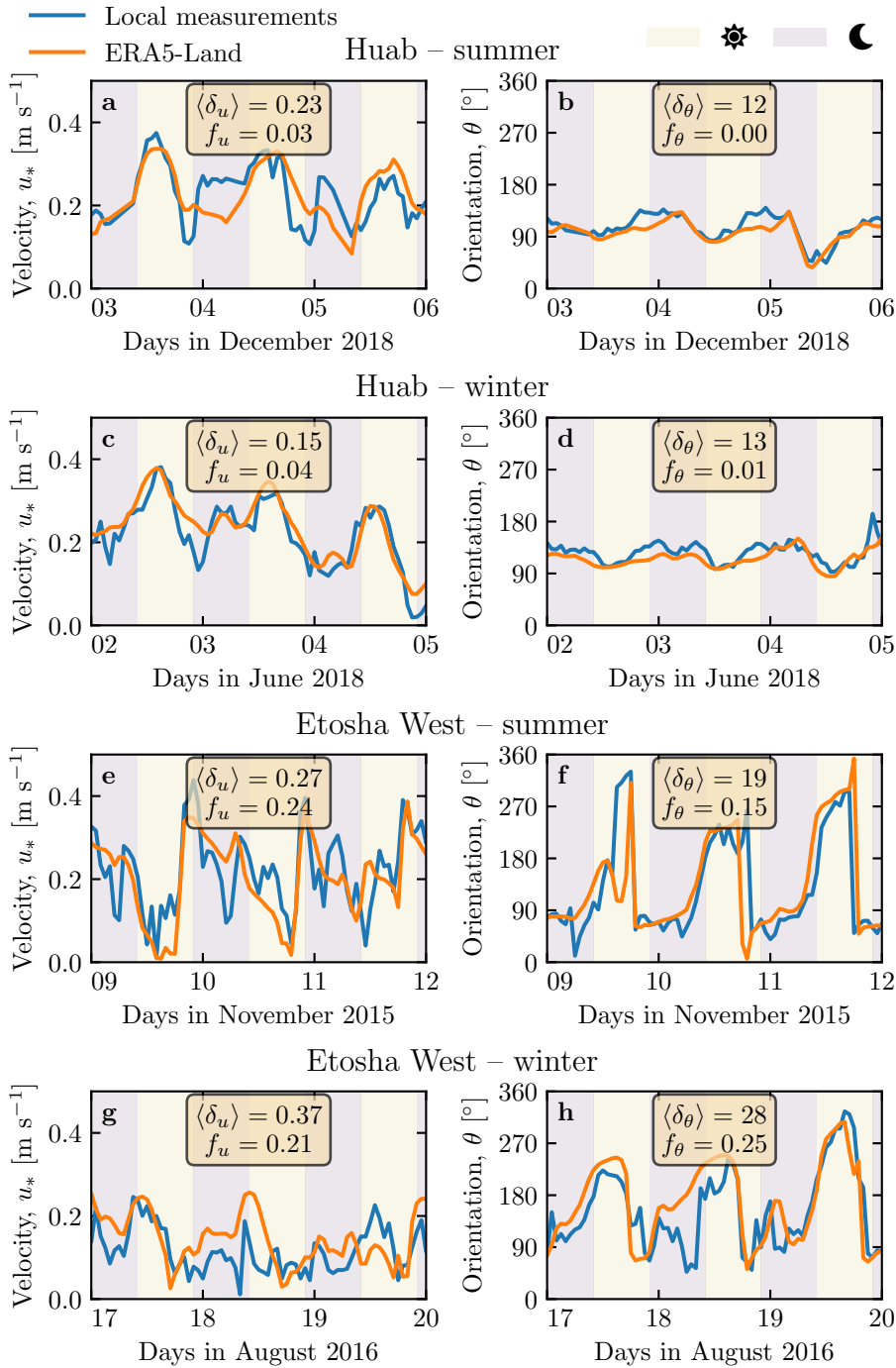


**Fig. 3** Temporal comparison between the wind data coming from the ERA5-Land climate reanalysis (orange lines) and from the local measurements (blue lines). Coloured swathes indicate day (between 10.00 UTC and 22.00 UTC) and night (before 10.00 UTC or after 22.00 UTC). Numbers in legends indicate the average flow deflection  $\delta_\theta$  and relative wind modulation  $\delta_u$  over the displayed period (see Sect. 3.2 for their definitions), as well as the percentage  $f_\theta$  and  $f_u$  of occurrence of extreme events ( $\delta_\theta > 50^\circ$ ,  $|\delta_u| > 0.6$ ). **a,b:** Huab station in summer. **b,c:** Huab station in winter. **d,e:** Etosha West station in summer. **f,g:** Etosha West station in winter. Time series of the two other stations are shown in Fig. 5.

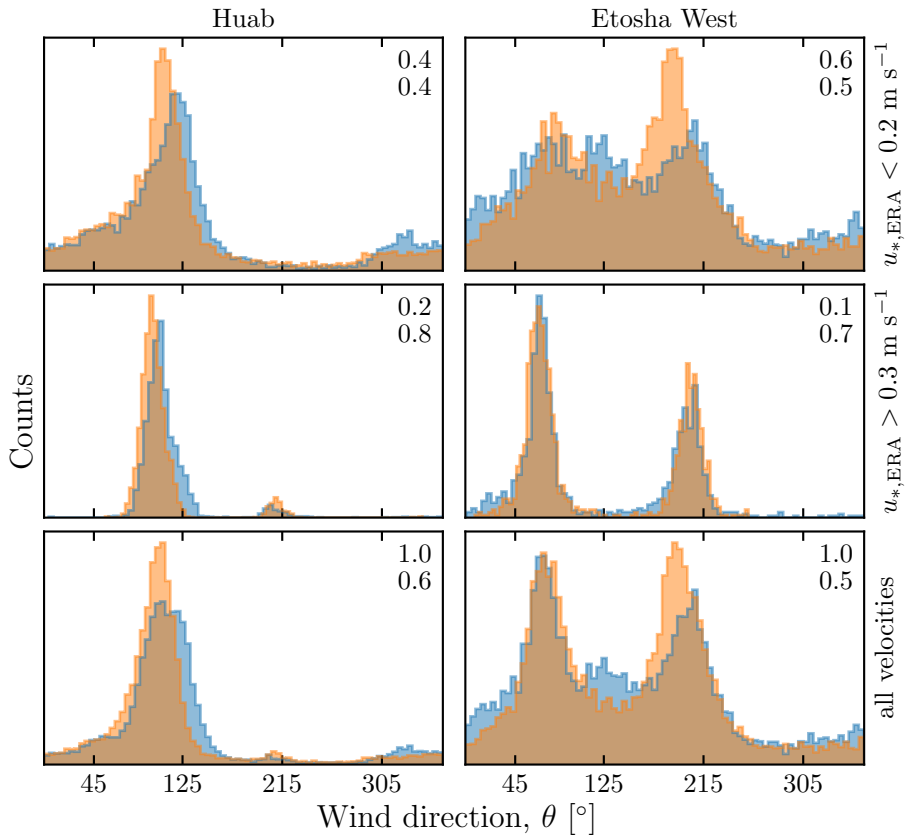


**Fig. 4** Distributions of wind direction at Huab and Etosha West stations for the ERA5-Land climate reanalysis (orange) and the local measurements (blue). In each subplot, both distributions are plotted from the same time steps, selected for different ranges of the wind wind velocity (rows) in the ERA5-Land dataset. The numbers at the upper right corners give the percentage of time steps selected in each sub-range (top), as well as the percentage of them corresponding to the day – defined between 10.00 UTC and 22.00 UTC (bottom).

which are responsible for the high wind velocities observed (Lancaster et al. 1984). The frequency of these easterly components decreases from inland to the coast. As a result, bidirectional wind regimes within the Namib Sand Sea and at the west Etosha site (Fig. 2a,c and d) and a unidirectional wind regime on the coast at the outlet of the Huab River (Fig. 2b) are observed.

In the case of the Etosha West and Huab stations, the time series of wind speed and direction from the regional predictions quantitatively match those corresponding to the local measurements (Figs. 3, 4 and Online Resource Fig. S5). For the North Sand Sea and South Sand Sea stations within the giant linear dune field, we observe that this agreement is also good, but limited to the October-March time period (Fig. 4a, b and e, f). However, the field-measured wind roses exhibit additional wind components aligned with the dune orientation, as evidenced on the satellite images (Fig. 2c and d).

More precisely, during the April–September period, the local and regional winds in the interdune match during daytime only, i.e when the southerly/southwesterly sea breeze dominates (Figs. 5c,d,g,h and 6). In the late afternoon and during the night, when the easterly ‘berg’ and katabatic winds blow, measurements and predictions differ. In this case, the angular wind distribution of the local measurements exhibits two additional modes corresponding to reversing winds aligned with the dune orientation (purple frame in Fig. 6, Online Resource Fig. S6). This deviation is also associated with a general attenuation of the wind strength (Online Resource Fig. S7). Remarkably, all these figures show that these wind reorientation and attenuation processes occur only at low velocities of the regional wind, typically for  $u_*^{\text{ERA5-Land}} \lesssim 0.2 \text{ m s}^{-1}$ . For shear velocities larger than  $u_*^{\text{ERA5-Land}} \simeq 0.3 \text{ m s}^{-1}$ , the wind reorientation is not apparent. Finally, for intermediate shear velocities, both situations of wind flow reoriented along the dune crest and not reoriented can be successively observed (Online Resource Fig. S6). Importantly, these values are not precise thresholds (and certainly not related to the threshold for sediment transport), but indicative of a crossover between regimes, whose physical interpretation is discussed in the next section.

### 3 Influence of Wind Speed and Circadian Cycle on the Atmospheric Boundary Layer

The wind deflection induced by dunes has previously been related to the incident angle between wind direction and crest orientation, with a maximum deflection evident for incident angles between  $30^\circ$  and  $70^\circ$  (Walker et al. 2009; Hesp et al. 2015). In the data analysed here, the most deflected wind at both the North and South Sand Sea stations is seen to be where the incident angle is perpendicular to the giant dunes (Figs. 2 and 6). It therefore appears that in our case, the incident wind angle is not the dominant control on maximum wind deflection. Further, and as shown in Fig. 6, winds of high and low velocities show contrasting behaviour in characteristics of deflection. This suggests a change in hydrodynamical regime between the winds. In this section, we discuss the relevant parameters associated with the dynamical mechanisms that govern the interactions between the atmospheric boundary layer flow and giant dune topographies. This analysis allows us to provide a physics-based interpretation of our measured wind data.

#### 3.1 Flow Over a Modulated Bed

Taking as a reference the turbulent flow over a flat bed, the general framework of our study is understanding and describing the flow response to a bed modulation (e.g. a giant dune). Without loss of generality, we can consider in this context an idealised bed elevation in the form of parallel sinusoidal ridges, with wavelength  $\lambda$  (or wavenumber  $k = 2\pi/\lambda$ ) and amplitude  $\xi_0$ , and where the reference flow direction makes a given incident angle with respect to the ridge

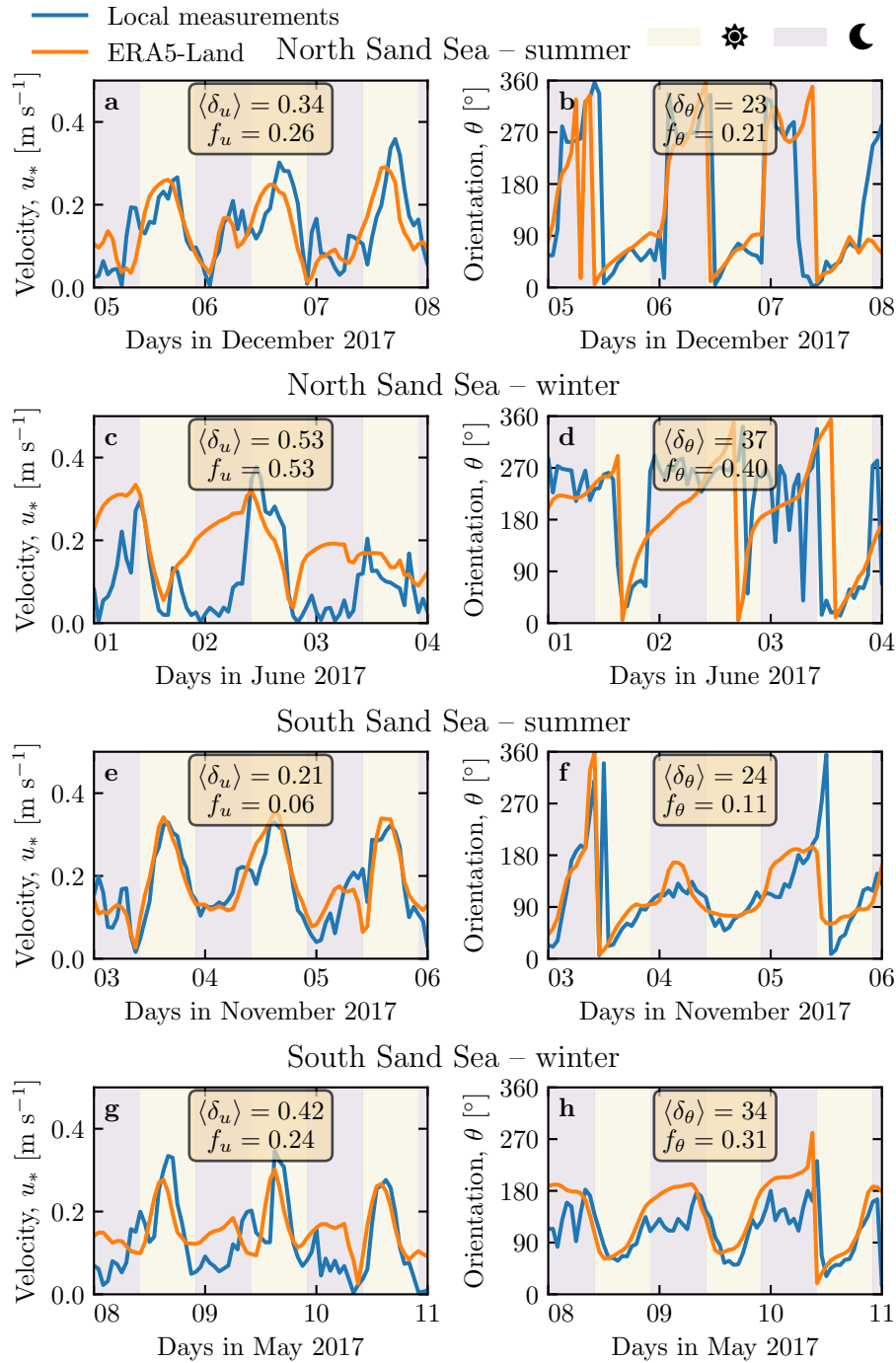


**Fig. 5** Same as Fig. 3 for North Sand Sea station in summer (a,b), North Sand Sea station in winter (b,c), South Sand Sea station in summer (d,e) and South Sand Sea station in winter (f,g).

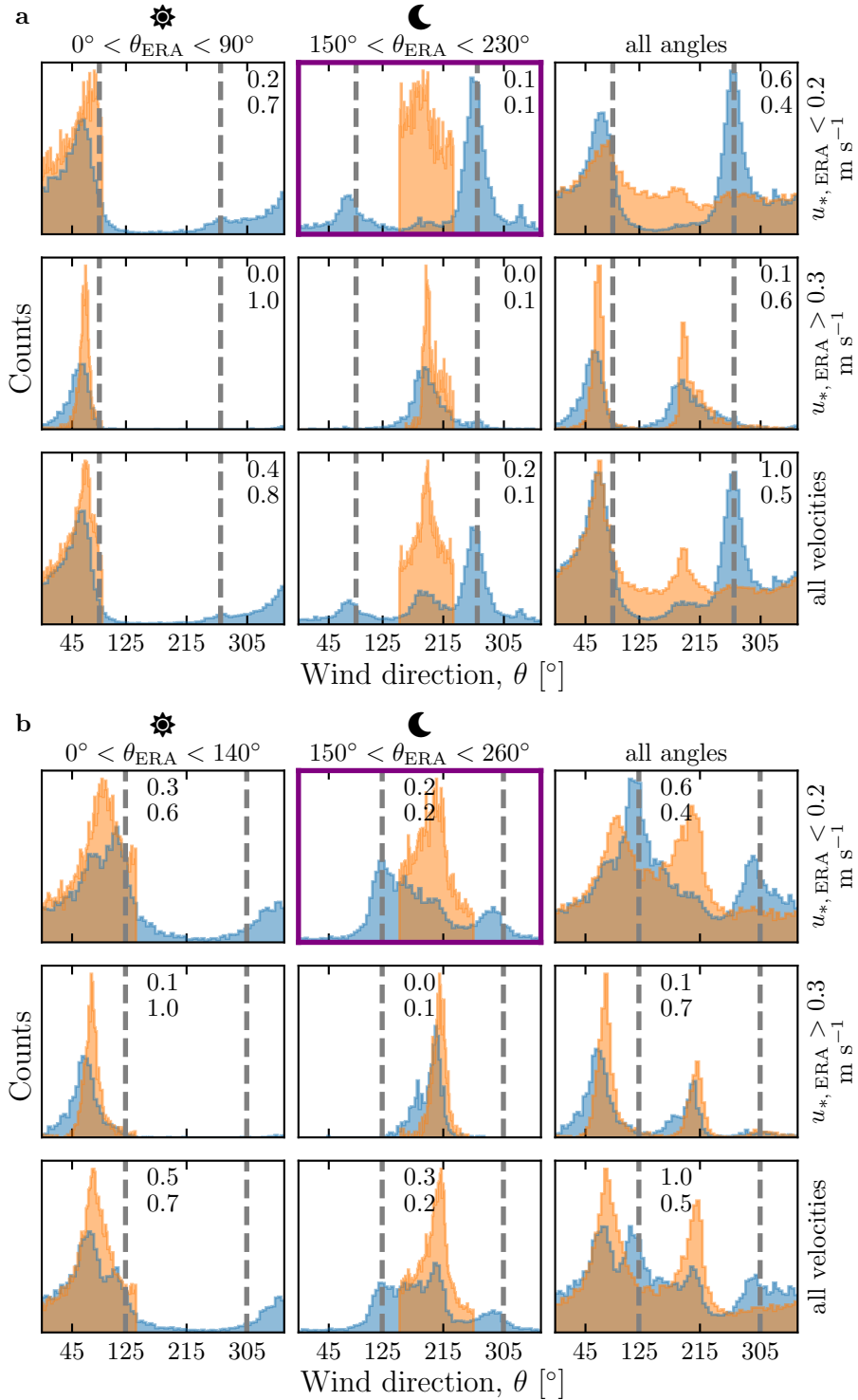


**Fig. 6** Same as Fig. 4 but for North Sand Sea (**a**) and South Sand Sea (**b**) stations. Here, subplots correspond to different ranges for the wind direction (columns) and wind velocity (rows) of the ERA5-Land dataset. The grey vertical dashed lines indicate the main dune orientation. In contrast with observations at the Huab and Etosha West stations (Fig. 4), histograms do not match well at low wind velocities, and the purple frame highlights the regime (low wind velocities, nocturnal easterly wind) in which the data from both datasets differ most.

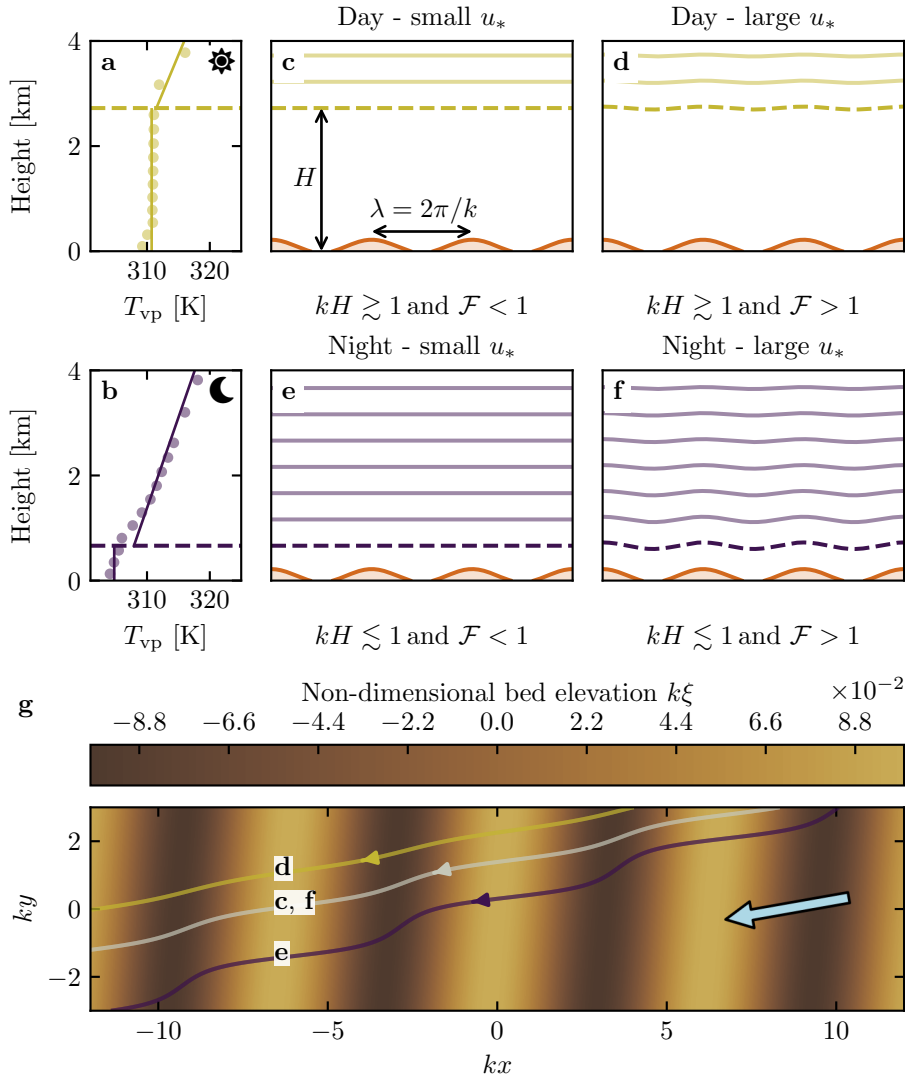


**Fig. 7** **a,b:** Vertical profiles of the virtual potential temperature  $T_{vp}$  at two different time steps (day - 03/11/2015 - 12.00 UTC, night - 01/13/2013 - 09.00 UTC) at the North Sand Sea station. Dots: data from the ERA5 reanalysis. Dashed lines: boundary layer height given by the ERA5 reanalysis (Online Resource section 2). Plain lines: vertical (boundary layer) and linear (free atmosphere) fits to estimate the stratification properties. **c–f:** Sketches representing the interaction between the giant dunes and the atmospheric flow for different meteorological conditions. **g:** Streamlines over a sinusoidal topography  $\xi(x, y)$  qualitatively representing the effect of low, medium and strong flow confinement, in relation to the above panels (see Appendix 4 for more details). The blue arrow indicates the undisturbed wind direction.

crest (Andreotti et al. 2012). Part of this response, on which we focus here, is the flow deflection by the ridges. In a simplified way, it can be understood from the Bernoulli principle (Hesp et al. 2015): as the flow approaches the ridge crest, the compression of the streamlines results in larger flow velocities, and thus lower pressures (Jackson and Hunt 1975). An incident flow oblique to the ridge is then deflected towards lower pressure zones, i.e. towards the crest. Turbulent dissipation tends to increase this effect downstream, resulting in wind deflection along the crest in the lee side (Gadal et al. 2019).

Flow confinement below a capping surface, which enhances streamline compression, has a strong effect on the hydrodynamic response and typically increases flow deflection. This is the case for bedforms forming in open channel flows such as rivers (Kennedy 1963; Chang and Simons 1970; Mizumura 1995; Colombini 2004; Fourrière et al. 2010; Andreotti et al. 2012; Unsworth et al. 2018). This is also relevant for aeolian dunes as they evolve in the turbulent atmospheric boundary layer (ABL) capped by the stratified free atmosphere (FA) (Andreotti et al. 2009). Two main mechanisms, associated with dimensionless numbers must then be considered (Fig. 7). First, topographic obstacles typically disturb the flow over a characteristic height similar to their length. As flow confinement is characterised by a thickness  $H$ , the interaction between the dunes and the wind in the ABL is well captured by the parameter  $kH$ . The height  $H$  is directly related to the sensitive heat flux from the Earth surface. It is typically on the order of a kilometre, but significantly varies with the circadian and seasonal cycles. Emerging and small dunes, with wavelengths in the range 20 to 100 m, are not affected by the flow confinement, corresponding to  $kH \gg 1$ . For giant dunes with kilometer-scale wavelengths, however, their interaction with the FA can be significant (Andreotti et al. 2009). This translates into a parameter  $kH$  in the range 0.02–5, depending on the moment of the day and the season. A second important mechanism is associated with the existence of a thin intermediate so-called capping layer between the ABL and the FA. It is characterised by a density jump  $\Delta\rho$ , which controls the ‘rigidity’ of this interface, i.e. how much its deformation affects streamline compression. This is usually quantified using the Froude number (Vosper 2004; Stull 2006; Sheridan and Vosper 2006; Hunt et al. 2006; Jiang 2014):

$$\mathcal{F} = \frac{U}{\sqrt{\frac{\Delta\rho}{\rho_0} g H}}, \quad (1)$$

where  $U$  is the wind velocity at the top of the ABL and  $\rho_0$  its average density. The intensity of the stratification, i.e. the amplitude of the gradient  $|\partial_z \rho|$  in the FA, also impacts the ability to deform the capping layer under the presence of an underlying obstacle, and thus affects the influence of flow confinement. This can be quantified using the internal Froude number (Vosper 2004; Stull 2006; Sheridan and Vosper 2006; Hunt et al. 2006; Jiang 2014)  $\mathcal{F}_I = kU/N$ , where  $N = \sqrt{-g\partial_z \rho / \rho_0}$  is the Brunt-Väisälä frequency (Stull 1988). Both Froude numbers have in practice the same qualitative effect on flow confinement (a

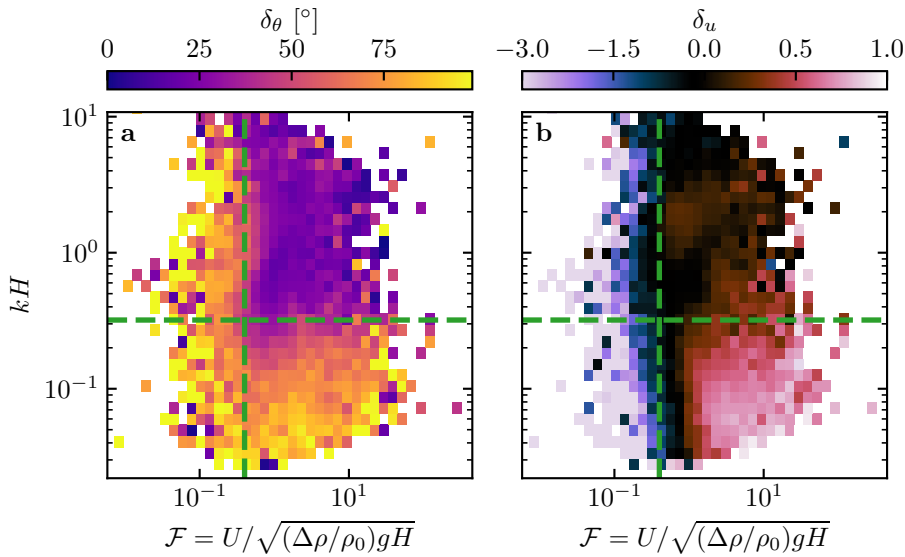


**Fig. 8** Regime diagrams of the wind deviation  $\delta_\theta$  (a) and relative attenuation/amplification  $\delta_u$  (b) in the space  $(\mathcal{F}, kH)$ , containing the data from both the North Sand Sea and South Sand Sea stations. The green dashed lines empirically delimit the different regimes. The point density in each bin of the diagrams is shown in Online Resource Fig. S10 – 95% of the data occur in the range  $-1 < \delta u < 1$ . Similar regime diagrams in the spaces  $(\mathcal{F}_I, kH)$  and  $(\mathcal{F}_I, \mathcal{F})$  are shown in Online Resource Fig. S11.

277 smaller Froude corresponding to a stiffer interface), and we shall restrict the  
278 main discussion to  $\mathcal{F}$  only.

279 With this theoretical framework in mind, and in the context of the mea-  
280 sured wind data in the North and South Sand Sea stations, the smallest wind  
281 disturbances are expected to occur during the day, when the ABL depth is the  
282 largest and comparable to the dune wavelength ( $kH \gtrsim 1$ ), which corresponds  
283 to a weak confinement situation (Fig. 7c and d). In contrast, large wind dis-  
284 turbances are expected to occur during the night, when the confinement is mainly  
285 induced by a shallow ABL (Fig. 7e). However, this strong confinement can be  
286 somewhat reduced in the case of strong winds, corresponding to large values of  
287 the Froude number and a less ‘rigid’ interface (Fig. 7f). This is in qualitative  
288 agreement with the transition from deflected to non-deflected winds related to  
289 low and high velocities observed in our data (Sec. 2.2).

### 290 3.2 Data Distribution in the Flow Regimes

291 We can go one step further and analyse how our data quantitatively spread  
292 over the different regimes discussed above. For that purpose, one needs to  
293 compute  $kH$  and  $\mathcal{F}$  from the time series.  $H$ ,  $U$  and the other atmospheric  
294 parameters can be deduced from the various vertical profiles (temperature,  
295 humidity) available in the ERA5 climate reanalysis (Online Resource section

296 2). We quantify the flow deflection  $\delta_\theta$  as the minimal angle between the wind  
 297 orientations comparing the local measurements and the regional predictions.  
 298 We also compute the relative velocity modulation as

$$\delta_u = \frac{u_*^{\text{ERA5-Land}} - u_*^{\text{Local mes.}}}{u_*^{\text{ERA5-Land}}}. \quad (2)$$

299 These two quantities are represented as maps in the plane  $(\mathcal{F}, kH)$  (Fig. 8a  
 300 and b), and one can clearly identify different regions in these plots. Small wind  
 301 disturbances (small  $\delta_\theta$  and  $\delta_u$ ) are located in the top-right part of the diagrams,  
 302 corresponding to a regime with low-interaction as well as low-confinement ( $kH$   
 303 and  $\mathcal{F}$  large enough, Fig. 7d). Lower values of  $kH$  (stronger interaction) or of  
 304 Froude number (stronger confinement) both lead to an increase in wind dis-  
 305 turbances, both in terms of orientation and velocity. Below a crossover value  
 306  $kH \simeq 0.3$ , wind disturbance is less sensitive to the  $\mathcal{F}$ -value. This is probably  
 307 due to enhanced non-linear effects linked to flow modulation by the obstacle  
 308 when confinement is strong (e.g. wakes and flow recirculations). The Froude  
 309 number also controls a transition from damped to amplified wind velocities  
 310 in the interdune, with a crossover around  $\mathcal{F} \simeq 0.4$  (Fig. 8b). Such an ampli-  
 311 fication is rather unexpected. Checking the occurrence of the corresponding  
 312 data, it appears that these amplifications are associated with the southerly  
 313 sea breeze, and occur dominantly during the October-March period, when the  
 314 other easterly wind is not present (Online Resource Fig. S12a–b). Further-  
 315 more, they occur less frequently during the afternoon, and more frequently  
 316 at the end of the day (Online Resource Fig. S12c). This effect may be linked  
 317 to a change in the flow behaviour in the lee side of the obstacles but further  
 318 measurements are needed in order to assess the different possibilities (Baines  
 319 1995; Vosper 2004).

320 As the hydrodynamic roughness  $z_0$  determine the magnitude of wind shear  
 321 velocities, Froude number  $\mathcal{F}$  and relative velocity modulation  $\delta_u$ , it is impor-  
 322 tant to discuss the sensitivity of the results to the  $z_0$ -values chosen for both the  
 323 ERA5-Land and the field data (see Online Resource Sect. 4). Other quanti-  
 324 ties associated with wind direction are independent of this choice. Considering  
 325 the possible range of realistic roughness values, the uncertainty on velocities  
 326 estimated using the law of the wall is at most 30 %. A similar maximum un-  
 327 certainty applies to the Froude number. This uncertainty also propagates to  
 328  $\delta_u$ , for which Figure S14 shows that the choice of roughness has little influence  
 329 on its temporal variations, even if it can induce a global increase or decrease  
 330 of its values. Hence, the choice of the  $z_0$ -values will not qualitatively affect  
 331 the overall aspect of the regime diagram presented in Figure 8b. It may only  
 332 change the value of  $\delta_u$  for which the transition between regimes is observed  
 333 (dashed green lines in Figure 8b). Our conclusions are thus robust with respect  
 334 to the somewhat arbitrary choice of the hydrodynamic roughness values.

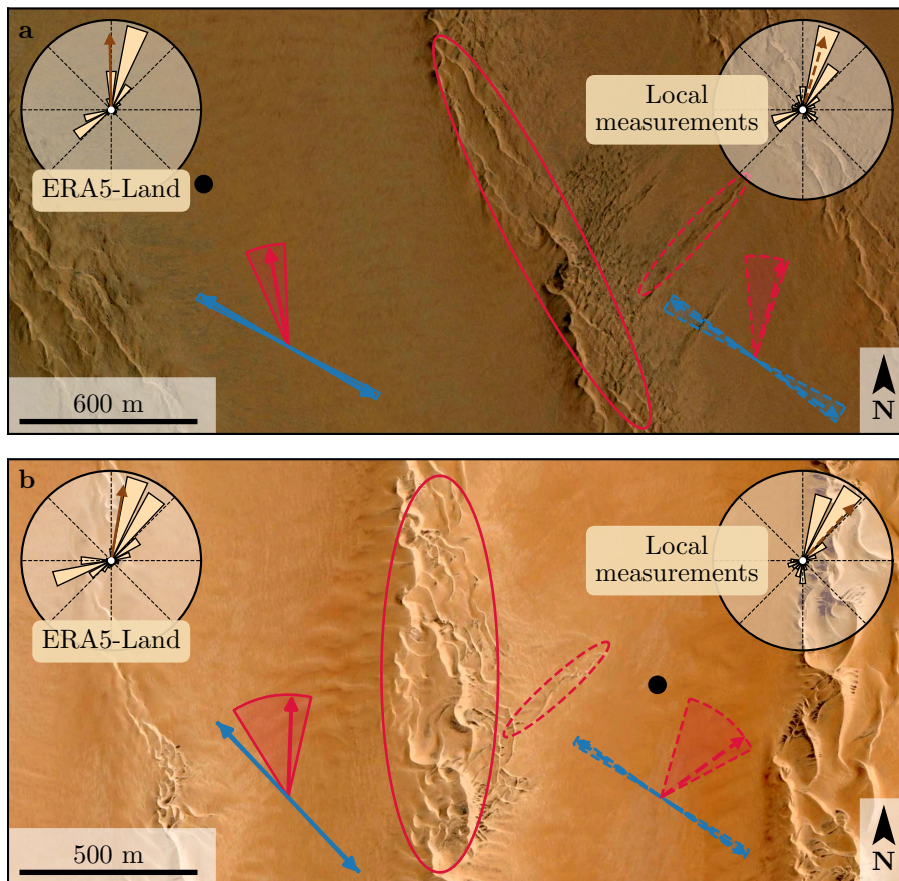


**Fig. 9** Implications for smaller scale patterns in (a) the South Sand Sea and (b) North Sand Sea. The ellipses indicate the different types of elongating dunes, at large (plain line) and small (dashed line) scales. Dune orientation are predicted using the model of Courrech du Pont et al. (2014) from the sand flux angular distributions, shown here (roses) along with the resultant transport direction (brown arrow) for typical values (grain size  $180 \mu\text{m}$ , flux-up ratio of 1.6). Code for corresponding arrows: use of ERA5-Land data (plain line), use of local measurements (dashed line), prediction for the bed instability growth mechanism (blue), prediction for the elongation growth mechanism (red). Wedges show the uncertainty on the orientation calculation when parameters are varied. The black dots indicate the location of the meteorological stations in the interdune. See Appendix 4 for additional details.

#### 335 4 Discussion and Conclusion

336 The feedback of the giant dunes on the wind flow has important implications  
 337 for smaller scale bedforms. As illustrated in Fig. 9, small linear dunes ( $\sim 50 \text{ m}$   
 338 wide) are often present within the 1–2 km interdune spaces between giant  
 339 linear dunes in the Namib Sand Sea (Livingstone et al. 2010). These smaller  
 340 dunes do not exhibit the same orientation as the large ones, and are sometimes  
 341 named ‘crossing dunes’ (Chandler et al. 2022). Whilst differences between large

and small scale dune patterns are observed ubiquitously, they are usually attributed to the presence of two different dune growth mechanisms, leading to two different dune patterns (orientations and/or morphologies) for the same wind regime (Courrech du Pont et al. 2014; Runyon et al. 2017; Lü et al. 2017; Song et al. 2019; Gadal et al. 2020; Hu et al. 2021). Here, however, our arguments enable the development of differing orientations for the small and giant linear dunes governed by the same dune growth mechanism (elongating mode). Figure 9 shows how the orientations for the small and giant dunes can be derived from the locally measured and regionally predicted winds respectively (red arrows in Fig. 9). These predictions require the threshold of aeolian sand transport to be specified. Importantly, its value (a shear velocity estimated at  $u_{th} \simeq 0.15 \text{ m s}^{-1}$  – see Appendix 4) can be reached in periods during which deflected winds are observed (recall that the stronger winds, responsible for most of the sediment transport and associated dune morphodynamics, are not deflected – see Fig. 6). The feedback of the giant dunes on the wind described in this study, through wind deflection and attenuation, thus provides a potential explanation for the existence of these small linear dunes elongating across the interdune, a dynamic which has remained unresolved to date. These crossing dunes could provide additional constraints for the inference of local winds from bedforms, similarly to that currently performed on Mars using ripple orientations (Liu and Zimbelman 2015; Hood et al. 2021). Further work is needed to investigate these processes in more detail, including measurements of sediment transport and flow on the top of dunes.

This study presents field and reanalysis-based evidence that wind flow patterns around giant dunes are influenced by the atmospheric boundary layer, particularly during nocturnal conditions. However, we do not address here the question of the limitation of the giant dune pattern coarsening, and leave open the debate as to whether their size is controlled by the depth of this layer (Andreotti et al. 2009), in contrast to sediment supply limited and ever-slower growth with size (Werner and Kocurek 1999; Gunn et al. 2022). More field evidence is definitively needed from additional dune fields, but this mechanism would allow for the inference of the ABL depth from giant bedform wavelengths where measurements are not feasible or available, such as Titan (Lorenz et al. 2010).

To conclude on conditions under which the ERA5-Land reanalysis data can reliably be used to study dune morphodynamics, we summarise the comparison of local (direct measurements) and regional (climate reanalysis) wind data as follows. In flat areas, the agreement between the two confirms the ability of the ERA5-Land climate reanalysis to predict the wind regime down to scales  $\sim 10 \text{ km}$ , i.e the model grid. When smaller scale topographies are present (giant dunes in our case), locally measured winds can significantly differ from the regionally predicted ones. This is the case when the disturbances induced by the dunes interact with the lower part of the ABL vertical structure, which presents circadian variations. During the day, when the capping layer is typically high, this interaction is small, and the ERA5-Land predictions are also quantitatively consistent with the local data. During the night, however, the

388 presence of a shallow atmospheric boundary layer induces a strong confinement  
389 of the flow, and is associated with large wind deflection by the dunes.  
390 Importantly, we find that this effect can be counterbalanced for large wind  
391 velocities, which are capable of deforming the capping layer, thus decreasing  
392 the influence of the confinement.

393 The theoretical computation of the wind disturbances induced by sinusoidal ridges under flow confinement has been performed in the linear limit  
394 (Andreotti et al. 2009, 2012), i.e. when the aspect ratio of these ridges is small  
395 ( $k\xi_0 \ll 1$ ). These models are able to qualitatively reproduce the observed  
396 wind deflection (Appendix 4, Online Resource Figs. S11 and S13), and thus  
397 provide the physical support for the interpretation we propose here based on  
398 hydrodynamic regimes. However, these models cannot quantitatively predict  
399 the magnitude of our observations, probably due to the presence of expected  
400 non-linearities in high confinement situations linked to strong flow modulations.  
401 Besides, these linear calculations only predict wind attenuation in the  
402 interdune, in contrast with the observed enhanced velocities associated with  
403 particular evening winds from the south during the period October–March  
404 (Online Resource Fig. S12). Some other models predict different spatial flow  
405 structures in response to a modulated topography, such as lee waves and  
406 rotors (Baines 1995; Vosper 2004). However, our measurements are located at a  
407 single point in the interdune, and we are thus unable to explore these types of  
408 responses. Data at different places along and across the ridges are needed to  
409 investigate and possibly map such flow structures, and for further comparisons  
410 with the models.

412 **Acknowledgements** We would like to acknowledge the contributors of the following open-  
413 source python libraries, Matplotlib (Hunter 2007), Numpy (Harris et al. 2020) and Scipy  
414 (Virtanen et al. 2020), which provide an incredibly efficient ecosystem allowing scientific  
415 research in Python. We also thank B. Andreotti and A. Gunn for useful discussions.

416 **Data Availability** All data used in this study can be found in Gadal et al. (2022). Note  
417 that it contains modified Copernicus Climate Change Service Information (2021). Neither  
418 the European Commission nor ECMWF is responsible for any use that may be made of  
419 the Copernicus Information or Data it contains. Documented codes used in this study to  
420 analyse this data are available at <https://github.com/Cgadal/GiantDunes> (will be made  
421 public upon acceptance of this manuscript for publication).

422 **Fundings** Multiple grants have supported the collection of wind data through visits to  
423 the four sites between 2013 and 2020 (John Fell Oxford University Press (OUP) Research  
424 Fund (121/474); National Geographic (CP-029R-17); Natural Environment Research Coun-  
425 cil UK (NE/R010196/1 and NE/H021841/1 NSFGEO-NERC); Southampton Marine and  
426 Maritime Institute SMMI EPSRC-GCRF UK), along with research permits (1978/2014,  
427 2140/2016, 2304/2017, 2308/2017, RPIV00022018, RPIV0052018, RPIV00230218). The au-  
428 thors are very grateful for support from Etosha National Park (especially Shyane Kötting,  
429 Boas Erckie, Pierre du Preez, Claudine Cloete, Immanuel Kapofi, Wilferd Versfeld, and  
430 Werner Kilian), Gobabeb Namib Research Institute (Gillian Maggs-Kölling and Eugene  
431 Marais), The Skeleton Coast National Park (Joshua Kazeurua). Various researchers and

desert enthusiasts have assisted with instruments and the logistics of expeditions, especially Mary Seely for expert guidance at the North Sand Sea site. Finally, we acknowledge financial support from the Laboratoire d'Excellence UnivEarthS Grant ANR-10-LABX-0023, the Initiative d'Excellence Université de Paris Grant ANR-18-IDEX-0001, the French National Research Agency Grants ANR-17-CE01-0014/SONO and the National Science Center of Poland Grant 2016/23/B/ST10/01700.

**Conflict of interest** The authors declare that they have no conflict of interest.

#### Appendix 1: Linear Theory of Wind Response to Topographic Perturbation

Following the work of Fourrière et al. (2010), Andreotti et al. (2012) and Andreotti et al. (2009), we briefly describe in this appendix the framework for the linear response of a turbulent flow to a topographic perturbation of small aspect ratio. As a general bed elevation can be decomposed into Fourier modes, we focus here on a sinusoidal topography:

$$\xi = \xi_0 \cos [k (\cos(\alpha)y - \sin(\alpha)x)], \quad (3)$$

which is also a good approximation for the giant dunes observed in the North Sand Sea and South Sand Sea Station (Fig. 2 and Online Resource Fig. S4). Here,  $x$  and  $y$  are the streamwise and spanwise coordinates,  $k = 2\pi/\lambda$  the wavenumber of the sinusoidal perturbation,  $\alpha$  its crest orientation with respect to the  $x$ -direction (anticlockwise) and  $\xi_0$  its amplitude. The two components of the basal shear stress  $\tau = \rho_0 u_* \mathbf{u}_*$ , constant in the flat bottom reference case, can then be generically written as:

$$\tau_x = \tau_0 \left( 1 + k \xi_0 \sqrt{\mathcal{A}_x^2 + \mathcal{B}_x^2} \cos [k (\cos(\alpha)y - \sin(\alpha)x) + \phi_x] \right), \quad (4)$$

$$\tau_y = \tau_0 k \xi_0 \sqrt{\mathcal{A}_y^2 + \mathcal{B}_y^2} \cos [k (\cos(\alpha)y - \sin(\alpha)x) + \phi_y], \quad (5)$$

where  $\tau_0$  is the reference basal shear stress on a flat bed. We have defined the phase  $\phi_{x,y} = \tan^{-1}(\mathcal{B}_{x,y}/\mathcal{A}_{x,y})$  from the in-phase and in-quadrature hydrodynamical coefficients  $\mathcal{A}_{x,y}$  and  $\mathcal{B}_{x,y}$ . They are functions of  $k$  and of the flow conditions, i.e the bottom roughness, the vertical flow structure and the incident flow direction, and the theoretical framework developed in the above cited papers proposes methods to compute them in the linear regime.

Following Andreotti et al. (2012), the effect of the incident wind direction can be approximated by the following expressions:

$$\mathcal{A}_x = \mathcal{A}_0 \sin^2 \alpha, \quad (6)$$

$$\mathcal{B}_x = \mathcal{B}_0 \sin^2 \alpha, \quad (7)$$

$$\mathcal{A}_y = -\frac{1}{2} \mathcal{A}_0 \cos \alpha \sin \alpha, \quad (8)$$

$$\mathcal{B}_y = -\frac{1}{2} \mathcal{B}_0 \cos \alpha \sin \alpha, \quad (9)$$

where  $\mathcal{A}_0$  and  $\mathcal{B}_0$  are now two coefficients independent of the dune orientation  $\alpha$ , corresponding to the transverse case ( $\alpha = 90$ ). In the case of a fully turbulent boundary layer capped by a stratified atmosphere, these coefficients depend on  $kH$ ,  $kz_0$ ,  $\mathcal{F}$  and  $\mathcal{F}_I$  (Andreotti et al. 2009). For their computation, we assume here a constant hydrodynamic roughness  $z_0 \simeq 1$  mm (Online Resource section 1). For the considered giant dunes, this leads to  $kz_0 \simeq 2 \cdot 10^{-6}$ , as their wavelength is  $\lambda \simeq 2.4$  km (or  $k \simeq 2 \cdot 10^{-3} \text{ m}^{-1}$ ). Values of  $z_0$  extracted from field data indeed typically fall between 0.1 mm and 10 mm (Sherman and Farrell 2008; Field and Pelletier 2018). Importantly,  $\mathcal{A}_0$  and  $\mathcal{B}_0$  do not vary much in the corresponding range of  $kz_0$  (Fourrière et al. 2010), and the results presented here are robust with respect to this choice.

With capping layer height and Froude numbers computed from the ERA5-Land time series, the corresponding  $\mathcal{A}_0$  and  $\mathcal{B}_0$  can be deduced, as displayed in Online Resource Fig. S13. Interestingly, it shows similar regimes as in the diagrams of Fig. 8 and Online Resource Fig. S11a,b, supporting the underlying physics. However, the agreement is qualitative only. Further, the linearity assumption of the theoretical framework requires  $(|\tau| - \tau_0)/\tau_0 \ll 1$ , which translates into  $k\xi\sqrt{\mathcal{A}_0^2 + \mathcal{B}_0^2} \ll 1$ . In our case, the giant dune morphology gives  $k\xi_0 \simeq 0.1$ , which means that one quits the regime of validity of the linear theory when the coefficient modulus  $\sqrt{\mathcal{A}_0^2 + \mathcal{B}_0^2}$  becomes larger than a few units. In accordance with the theoretical expectations, these coefficients present values on the order of unity ( $\mathcal{A}_0 \simeq 3$  and  $\mathcal{B}_0 \simeq 1$ ) in unconfined situations (Claudin et al. 2013; Lü et al. 2021). In contrast and as illustrated in Online Resource Fig. S13a,b, larger values are predicted in case of strong confinement, which does not allow us to proceed to further quantitative comparison with the data.

Finally, the linear model is also able to reproduce the enhancement of the flow deflection over the sinusoidal ridges when  $\sqrt{\mathcal{A}_0^2 + \mathcal{B}_0^2}$  is increased (Online Resource Fig. S13). Here, using  $k\xi_0 \simeq 0.1$  to be representative of the amplitude of the giant dunes at the North Sand Sea station, the coefficient modulus is bounded to 10.

## Appendix 2: Sediment Transport and Dune Morphodynamics

We summarise in this appendix the sediment transport and dune morphodynamics theoretical framework leading to the prediction of sand fluxes and dune orientations from wind data.

*Sediment Transport* — The prediction of sand fluxes from wind data has been a long standing issue in aeolian geomorphological studies (Fryberger and Dean 1979; Pearce and Walker 2005; Sherman and Li 2012; Shen et al. 2019). Based on laboratory studies in wind tunnels (Rasmussen et al. 1996; Iversen and Rasmussen 1999; Creyssels et al. 2009; Ho et al. 2011), as well as physical considerations (Ungar and Haff 1987; Andreotti 2004; Durán et al. 2011; Pähzt

and Durán 2020), it has been shown that the steady saturated saltation flux over a flat sand bed depends linearly on the shear stress:

$$\frac{q_{\text{sat}}}{Q} = \Omega \sqrt{\Theta_{\text{th}}} (\Theta - \Theta_{\text{th}}), \quad (10)$$

where  $\Omega$  is a proportionality constant,  $Q = d\sqrt{(\rho_s - \rho_0)gd/\rho_0}$  is a characteristic flux,  $\Theta = \rho_0 u_*^2 / (\rho_s - \rho_0)gd$  the Shields number, and  $\Theta_{\text{th}}$  its threshold value below which saltation vanishes.  $\rho_s = 2.6 \text{ g cm}^{-3}$  and  $d = 180 \mu\text{m}$  are the grain density and diameter, and  $g$  is the gravitational acceleration. The shear velocity, and consequently the Shields number as well as the sediment flux, are time dependent.

Recently, Pähzt and Durán (2020) suggested an additional quadratic term in Shields to account for grain-grain interactions within the transport layer at strong wind velocities:

$$\frac{q_{\text{sat}, t}}{Q} = \frac{2\sqrt{\Theta_{\text{th}}}}{\kappa\mu} (\Theta - \Theta_{\text{th}}) \left( 1 + \frac{C_M}{\mu} [\Theta - \Theta_{\text{th}}] \right), \quad (11)$$

where  $\kappa = 0.4$  is the von Kármán constant,  $C_M \simeq 1.7$  a constant and  $\mu \simeq 0.6$  is a friction coefficient, taken to be the avalanche slope of the granular material. The fit of this law to the experimental data of Creyssels et al. (2009) and Ho et al. (2011) gives  $\Theta_{\text{th}} = 0.0035$ . The fit of Eq. 10 on these same data similarly gives  $\Omega \simeq 8$  and  $\Theta_{\text{th}} = 0.005$ . The sand flux angular distributions and the dune orientations in Fig. 9 are calculated using this law (11). We have checked that using the ordinary linear relationship (10) instead does not change the predicted dune orientations by more than a few degrees.

*Dune Orientations* — Dune orientations are predicted with the dimensional model of Courrech du Pont et al. (2014), from the sand flux time series computed with the above transport law. Two orientations are possible depending on the mechanism dominating the dune growth: elongation or bed instability. The orientation  $\alpha$  corresponding to the bed instability is then the one that maximises the following growth rate (Rubin and Hunter 1987):

$$\sigma \propto \frac{1}{H_d W_d T} \int_0^T q_{\text{crest}} |\sin(\theta - \alpha)| dt, \quad (12)$$

where  $\theta$  is the wind orientation measured with respect to the same reference as  $\alpha$ , and  $H_d$  and  $W_d$  are dimensional constants respectively representing the dune height and width. The integral runs over a time  $T$ , which must be representative of the characteristic period of the wind regime. The flux at the crest is expressed as:

$$q_{\text{crest}} = q_{\text{sat}} [1 + \gamma |\sin(\theta - \alpha)|], \quad (13)$$

where the flux-up ratio  $\gamma$  has been calibrated to 1.6 using field studies, underwater laboratory experiments and numerical simulations. Predictions of the linear analysis of Gadal et al. (2019) and Delorme et al. (2020) give similar results.

<sup>536</sup> Similarly, the dune orientation corresponding to the elongation mechanism  
<sup>537</sup> is the one that verifies:

$$\tan(\alpha) = \frac{\langle q_{\text{crest}}(\alpha) \mathbf{e}_\theta \rangle \cdot \mathbf{e}_{WE}}{\langle q_{\text{crest}}(\alpha) \mathbf{e}_\theta \rangle \cdot \mathbf{e}_{SN}}, \quad (14)$$

<sup>538</sup> where  $\langle \cdot \rangle$  denotes a vectorial time average. The unitary vectors  $\mathbf{e}_{WE}$ ,  $\mathbf{e}_{SN}$  and  
<sup>539</sup>  $\mathbf{e}_\theta$  are in the West-East, South-North and wind directions, respectively.

<sup>540</sup> The resulting computed dune orientations, blue and red arrows in Fig. 9,  
<sup>541</sup> then depend on a certain number of parameters (grain properties, flux-up ratio,  
<sup>542</sup> etc.), for which we take typical values for aeolian sandy deserts. Due to the lack  
<sup>543</sup> of measurements in the studied places, some uncertainties can be expected. We  
<sup>544</sup> therefore run a sensitivity test by calculating the dune orientations for grain  
<sup>545</sup> diameters ranging from 100  $\mu\text{m}$  to 400  $\mu\text{m}$  and for a speed-up ratio between  
<sup>546</sup> 0.1 and 10 (wedges in Fig. 9).

---

**547 References**

- 548 Andreotti B (2004) A two-species model of aeolian sand transport. *J Fluid  
549 Mech* 510:47–70
- 550 Andreotti B, Claudin P, Douady S (2002) Selection of dune shapes and veloc-  
551 ities part 1: dynamics of sand, wind and barchans. *The European Physical  
552 Journal B-Condensed Matter and Complex Systems* 28:321–339
- 553 Andreotti B, Fourrière A, Ould-Kaddour F, Murray B, Claudin P (2009) Gi-  
554 ant aeolian dune size determined by the average depth of the atmospheric  
555 boundary layer. *Nature* 457:1120–1123
- 556 Andreotti B, Claudin P, Devauchelle O, Durán O, Fourrière A (2012) Bedforms  
557 in a turbulent stream: ripples, chevrons and antidunes. *J Fluid Mech* 690:94–  
558 128
- 559 Ashkenazy Y, Yizhaq H, Tsoar H (2012) Sand dune mobility under climate  
560 change in the kalahari and australian deserts. *Climatic Change* 112:901–923
- 561 Baddock M, Livingstone I, Wiggs G (2007) The geomorphological significance  
562 of airflow patterns in transverse dune interdunes. *Geomorphology* 87:322–  
563 336
- 564 Bagnold RA (1941) *The Physics of Blown Sand and Desert Dunes*. London :  
565 Methuen : Chapman & Hall
- 566 Baines PG (1995) Topographic effects in stratified flows. Cambridge university  
567 press
- 568 Bauer BO, Sherman DJ, Wolcott JF (1992) Sources of uncertainty in shear  
569 stress and roughness length estimates derived from velocity profiles. *The  
570 Professional Geographer* 44:453–464
- 571 Belcher S, Hunt J (1998) Turbulent flow over hills and waves. *Annu Rev Fluid  
572 Mech* 30:507–538
- 573 Blumberg DG, Greeley R (1996) A comparison of general circulation model  
574 predictions to sand drift and dune orientations. *J Clim* 9:3248–3259
- 575 Bristow NR, Best J, Wiggs GFS, Nield JM, Baddock MC, Delorme P, Chris-  
576 tensen KT (2022) Topographic perturbation of turbulent boundary layers  
577 by low-angle, early-stage aeolian dunes. *Earth Surf Process Landf* n/a, DOI  
578 <https://doi.org/10.1002/esp.5326>
- 579 Brookfield M (1977) The origin of bounding surfaces in ancient aeolian sand-  
580 stones. *Sedimentology* 24:303–332
- 581 Brown S, Nickling WG, Gillies JA (2008) A wind tunnel examination of shear  
582 stress partitioning for an assortment of surface roughness distributions. *J  
583 Geophys Res* 113:F02S06
- 584 Chandler C, Radebaugh J, McBride J, Morris T, Narteau C, Arnold K, Lorenz  
585 R, Barnes J, Hayes A, Rodriguez S, Rittenour T (2022) Near-surface struc-  
586 ture of a large linear dune and an associated crossing dune of the northern  
587 Namib Sand Sea from ground penetrating radar: Implications for the his-  
588 tory of large linear dunes on Earth and Titan. *Aeolian Research* 57:100813,  
589 DOI <https://doi.org/10.1016/j.aeolia.2022.100813>
- 590 Chang H, Simons D (1970) The bed configuration of straight sand-bed channels  
591 when flow is nearly critical. *J Fluid Mech* 42:491–495

- 592 Charru F, Andreotti B, Claudin P (2013) Sand ripples and dunes. *Annu Rev Fluid Mech* 45:469–493
- 593
- 594 Claudin P, Wiggs G, Andreotti B (2013) Field evidence for the upwind velocity shift at the crest of low dunes. *Boundary-Layer Meteorol* 148:195–206
- 595
- 596 Claudin P, Durán O, Andreotti B (2017) Dissolution instability and roughening transition. *J Fluid Mech* 832:R2
- 597
- 598 Claudin P, Louge M, Andreotti B (2021) Basal pressure variations induced by a turbulent flow over a wavy surface. *Frontiers in Physics* 9:682564
- 599
- 600 Colombini M (2004) Revisiting the linear theory of sand dune formation. *J Fluid Mech* 502:1–16
- 601
- 602 Courrech du Pont S (2015) Dune morphodynamics. *C R Phys* 16:118–138
- 603 Courrech du Pont S, Narteau C, Gao X (2014) Two modes for dune orientation. *Geology* 42:743–746
- 604
- 605 Creyssels M, Dupont P, El Moctar AO, Valance A, Cantat I, Jenkins JT, Pasini JM, Rasmussen KR (2009) Saltating particles in a turbulent boundary layer: experiment and theory. *J Fluid Mech* 625:47–74
- 606
- 607 de Winter W, Donker J, Sterk G, Van Beem J, Ruessink G (2020) Regional versus local wind speed and direction at a narrow beach with a high and steep foredune. *Plos one* 15:e0226983
- 608
- 609 Dee DP, Uppala SM, Simmons AJ, Berrisford P, Poli P, Kobayashi S, Andrae U, Balmaseda M, Balsamo G, Bauer dP, et al. (2011) The ERA-Interim reanalysis: Configuration and performance of the data assimilation system. *Q J R Meteorol Soc* 137:553–597
- 610
- 611 Delorme P, Wiggs G, Baddock M, Claudin P, Nield J, Valdez A (2020) Dune initiation in a bimodal wind regime. *J Geophys Res* 125:e2020JF005757
- 612
- 613 Durán O, Claudin P, Andreotti B (2011) On aeolian transport: Grain-scale interactions, dynamical mechanisms and scaling laws. *Aeolian Res* 3:243–270
- 614
- 615 Durran DR (1990) Mountain waves and downslope winds. In: *Atmospheric processes over complex terrain*, Springer, pp 59–81
- 616
- 617 Dyer A (1974) A review of flux-profile relationships. *Boundary-Layer Meteorol* 7:363–372
- 618
- 619 Ewing RC, Kocurek G, Lake LW (2006) Pattern analysis of dune-field parameters. *Earth Surf Process Landf* 31:1176–1191
- 620
- 621 Farr TG, Rosen PA, Caro E, Crippen R, Duren R, Hensley S, Kobrick M, Paller M, Rodriguez E, Roth L, et al. (2007) The shuttle radar topography mission. *Rev Geophys* 45
- 622
- 623 Fernando H, Mann J, Palma J, Lundquist JK, Barthelmie RJ, Belo-Pereira M, Brown W, Chow F, Gerz T, Hocut C, et al. (2019) The perdigão: Peering into microscale details of mountain winds. *Bull Am Meteorol Soc* 100:799–819
- 624
- 625 Field JP, Pelletier JD (2018) Controls on the aerodynamic roughness length and the grain-size dependence of aeolian sediment transport. *Earth Surf Process Landf* 43:2616–2626
- 626
- 627 Finnigan J, Raupach M, Bradley E, Aldis G (1990) A wind tunnel study of turbulent flow over a two-dimensional ridge. *Boundary-Layer Meteorol*
- 628
- 629
- 630
- 631
- 632
- 633
- 634
- 635
- 636
- 637

- 638 50:277–317
- 639 Finnigan J, Ayotte K, Harman I, Katul G, Oldroyd H, Patton E, Poggi D,  
640 Ross A, Taylor P (2020) Boundary-layer flow over complex topography.  
Boundary-Layer Meteorol 177:247–313
- 642 Flack K, Schultz M (2010) Review of hydraulic roughness scales in the fully  
643 rough regime. Journal of Fluids Engineering 132:041203
- 644 Fourrière A, Claudin P, Andreotti B (2010) Bedforms in a turbulent stream:  
645 formation of ripples by primary linear instability and of dunes by nonlinear  
646 pattern coarsening. J Fluid Mech 649:287–328
- 647 Frederick KA, Hanratty TJ (1988) Velocity measurements for a turbulent non-  
648 separated flow over solid waves. Exp Fluids 6:477–486
- 649 Fryberger SG, Dean G (1979) Dune forms and wind regime. A study of global  
650 sand seas 1052:137–169
- 651 Gadal C, Narteau C, Courrech Du Pont S, Rozier O, Claudin P (2019) Incip-  
652 ient bedforms in a bidirectional wind regime. J Fluid Mech 862:490–516
- 653 Gadal C, Narteau C, Courrech du Pont S, Rozier O, Claudin P (2020) Peri-  
654 odicity in fields of elongating dunes. Geology 48:343–347
- 655 Gadal C, Delorme P, Narteau C, Wiggs G, Baddock M, Nield JM, Claudin  
656 P (2022) Data used in 'Local wind regime induced by giant linear dunes:  
657 comparison of ERA5-Land re-analysis with surface measurements'. DOI  
658 10.5281/zenodo.6343138
- 659 Gao X, Narteau C, Gadal C (2021) Migration of reversing dunes against the  
660 sand flow path as a singular expression of the speed-up effect. Journal of  
661 Geophysical Research: Earth Surface 126(5):e2020JF005913
- 662 Garratt JR (1994) The atmospheric boundary layer. Earth-Science Reviews  
663 37:89–134
- 664 Garvey B, Castro IP, Wiggs G, Bullard J (2005) Measurements of flows over  
665 isolated valleys. Boundary-Layer Meteorol 117:417–446
- 666 Gong W, Ibbetson A (1989) A wind tunnel study of turbulent flow over model  
667 hills. Boundary-Layer Meteorol 49:113–148
- 668 Gong W, Taylor P, Dörnbrack A (1996) Turbulent boundary-layer flow over  
669 fixed aerodynamically rough two-dimensional sinusoidal waves. J Fluid Mech  
670 312:1–37
- 671 Guérin A, Derr J, Du Pont SC, Berhanu M (2020) Streamwise dissolution  
672 patterns created by a flowing water film. Phys Rev Lett 125:194502
- 673 Gunn A, Wanker M, Lancaster N, Edmonds D, Ewing R, Jerolmack  
674 D (2021) Circadian rhythm of dune-field activity. Geophys Res Lett  
675 48:e2020GL090924
- 676 Gunn A, Casasanta G, Di Liberto L, Falcini F, Lancaster N, Jerolmack DJ  
677 (2022) What sets aeolian dune height? Nature communications 13(1):1–8
- 678 Harris CR, Millman KJ, van der Walt SJ, Gommers R, Virtanen P, Cournapeau  
679 D, Wieser E, Taylor J, Berg S, Smith NJ, et al. (2020) Array program-  
680 ming with numpy. Nature 585:357–362
- 681 Havholm KG, Kocurek G (1988) A preliminary study of the dynamics of  
682 a modern draa, Algodones, southeastern California, USA. Sedimentology  
683 35:649–669

- 684 Hersbach H, Bell B, Berrisford P, Hirahara S, Horányi A, Muñoz-Sabater J,  
685 Nicolas J, Peubey C, Radu R, Schepers D, et al. (2020) The ERA5 global  
686 reanalysis. *Q J R Meteorol Soc* 146:1999–2049
- 687 Hesp P, Illenberger W, Rust I, McLachlan A, Hyde R (1989) Some aspects of  
688 transgressive dunefield and transverse dune geomorphology and dynamics,  
689 south coast, South Africa. *Zeitschrift fur Geomorphologie*, Supplementband  
690 73:111–123
- 691 Hesp PA, Hastings K (1998) Width, height and slope relationships and aero-  
692 dynamic maintenance of barchans. *Geomorphology* 22:193–204
- 693 Hesp PA, Smyth TAG, Nielsen P, Walker IJ, Bauer BO, Davidson-Arnott R  
694 (2015) Flow deflection over a foredune. *Geomorphology* 230:64–74
- 695 Ho TD, Valance A, Dupont P, Ould El Moctar A (2011) Scaling laws in aeolian  
696 sand transport. *Phys Rev Lett* 106:4–7
- 697 Hood DR, Ewing RC, Roback KP, Runyon K, Avouac JP, McEnroe M (2021)  
698 Inferring airflow across martian dunes from ripple patterns and dynamics.  
699 *Frontiers in Earth Science* 9:702828
- 700 Howard AD (1977) Effect of slope on the threshold of motion and its applica-  
701 tion to orientation of wind ripples. *Geological Society of America Bulletin*  
702 88:853–856
- 703 Hu Z, Gao X, Lei J, Zhou N (2021) Geomorphology of aeolian dunes in the  
704 western Sahara Desert. *Geomorphology* 392:107916
- 705 Hunt J, Leibovich S, Richards K (1988) Turbulent shear flows over low hills.  
706 *Q J R Meteorol Soc* 114:1435–1470
- 707 Hunt JCR, Vilenski GG, Johnson ER (2006) Stratified separated flow around  
708 a mountain with an inversion layer below the mountain top. *J Fluid Mech*  
709 556:105–119
- 710 Hunter JD (2007) Matplotlib: A 2d graphics environment. *Computing in sci-  
711 ence & engineering* 9:90–95
- 712 Hunter RE, Richmond BM, Alpha TR (1983) Storm-controlled oblique dunes  
713 of the Oregon coast. *Geol Soc America Bull* 94:1450–1465
- 714 Iversen JD, Rasmussen KR (1999) The effect of wind speed and bed slope on  
715 sand transport. *Sedimentology* 46:723–731
- 716 Jackson PS, Hunt JCR (1975) Turbulent wind flow over a low hill. *Q J R  
717 Meteorol Soc* 101:929–955
- 718 Jiang Q (2014) Applicability of reduced-gravity shallow-water theory to atmo-  
719 spheric flow over topography. *J Atmos Sci* 71:1460–1479
- 720 Jolivet M, Braucher R, Dovchintseren D, Hocquet S, Schmitt J, ASTER Team  
721 (2021) Erosion around a large-scale topographic high in a semi-arid sedimen-  
722 tary basin: Interactions between fluvial erosion, aeolian erosion and aeolian  
723 transport. *Geomorphology* 386:107747
- 724 Kennedy JF (1963) The mechanics of dunes and antidunes in erodible-bed  
725 channels. *J Fluid Mech* 16:521–544
- 726 Kim HG, Patel VC, Lee CM (2000) Numerical simulation of wind flow over  
727 hilly terrain. *J Wind Eng Ind Aerodyn* 87:45–60
- 728 Kroy K, Sauermann G, Herrmann HJ (2002) Minimal model for aeolian sand  
729 dunes. *Phys Rev E* 66:031302

- 730 Lancaster J, Lancaster N, Seely M (1984) Climate of the central Namib desert.  
731 Madoqua 1984:5–61
- 732 Lancaster N (1985) Winds and sand movements in the Namib sand sea. *Earth  
733 Surf Process Landf* 10:607–619
- 734 Lancaster N, Nickling W, Neuman CM, Wyatt V (1996) Sediment flux and  
735 airflow on the stoss slope of a barchan dune. *Geomorphology* 17:55–62
- 736 Lewis HW, Mobbs SD, Lehning M (2008) Observations of cross-ridge flows  
737 across steep terrain. *Q J R Meteorol Soc* 134:801–816
- 738 Liu ZYC, Zimbelman JR (2015) Recent near-surface wind directions inferred  
739 from mapping sand ripples on martian dunes. *Icarus* 261:169–181
- 740 Livingstone I, Warren A (2019) Aeolian geomorphology: a new introduction.  
741 Wiley
- 742 Livingstone I, Bristow C, Bryant RG, Bullard J, White K, Wiggs GFS, Baas  
743 ACW, Bateman MD, Thomas DSG (2010) The Namib Sand Sea digital  
744 database of aeolian dunes and key forcing variables. *Aeolian Res* 2:93–104
- 745 Lorenz R, Claudin P, Andreotti B, Radebaugh J, Tokano T (2010) A 3 km at-  
746 mospheric boundary layer on Titan indicated by dune spacing and Huygens  
747 data. *Icarus* 205:719–721
- 748 Lü P, Narteau C, Dong Z, Rozier O, Du Pont SC (2017) Unravelling raked  
749 linear dunes to explain the coexistence of bedforms in complex dunefields.  
750 *Nature Communications* 8:1–9
- 751 Lü P, Narteau C, Dong Z, Claudin P, Rodriguez S, An Z, Fernandez-Cascales  
752 L, Gadal C, Courrech du Pont S (2021) Direct validation of dune instability  
753 theory. *Proceedings of the National Academy of Sciences* 118
- 754 Mason P, Sykes R (1979) Flow over an isolated hill of moderate slope. *Q J R  
755 Meteorol Soc* 105:383–395
- 756 McKenna Neuman C, Lancaster N, Nickling WG (1997) Relations between  
757 dune morphology, air flow, and sediment flux on reversing dunes, Silver Peak,  
758 Nevada. *Sedimentology* 44:1103–1111, DOI 10.1046/j.1365-3091.1997.d01-  
759 61.x
- 760 Mizumura K (1995) Free-surface profile of open-channel flow with wavy bound-  
761 ary. *J Hydraul Eng* 121:533–539
- 762 Monin AS, Obukhov AM (1954) Basic laws of turbulent mixing in the surface  
763 layer of the atmosphere. *Contrib Geophys Inst Acad Sci USSR* 151:e187
- 764 Mulligan KR (1988) Velocity profiles measured on the windward slope of a  
765 transverse dune. *Earth Surf Process Landf* 13:573–582
- 766 Muñoz-Sabater J, Dutra E, Agustí-Panareda A, Albergel C, Arduini G, Bal-  
767 samo G, Boussetta S, Choulga M, Harrigan S, Hersbach H, et al. (2021)  
768 ERA5-Land: A state-of-the-art global reanalysis dataset for land applica-  
769 tions. *Earth Syst Sci Data* 13:4349–4383
- 770 Nield JM, King J, Wiggs GFS, Leyland J, Bryant RG, Chiverrell RC, Darby  
771 SE, Eckhardt FD, Thomas DSG, Vircavs LH, Washington R (2014) Esti-  
772 mating aerodynamic roughness over complex surface terrain. *J Geophys Res*  
773 118:12948–12961
- 774 Nield JM, Wiggs GG, Baddock MC, Hipondoka MH (2017) Coupling lee-  
775 side rainfall to avalanche characteristics in aeolian dune dynamics. *Geology*

- 776 45:271–274
- 777 Pähzt T, Durán O (2020) Unification of aeolian and fluvial sediment transport  
778 rate from granular physics. *Phys Rev Lett* 124:168001
- 779 Pearce KI, Walker IJ (2005) Frequency and magnitude biases in the 'Fryberger'  
780 model, with implications for characterizing geomorphically effective winds.  
781 *Geomorphology* 68:39–55
- 782 Pelletier JD, Field JP (2016) Predicting the roughness length of turbulent flows  
783 over landscapes with multi-scale microtopography. *Earth Surface Dynamics*  
784 4:391–405
- 785 Poggi D, Katul G, Albertson J, Ridolfi L (2007) An experimental investigation  
786 of turbulent flows over a hilly surface. *Phys Fluids* 19:036601
- 787 Rasmussen KR (1989) Some aspects of flow over coastal dunes. *Proceedings of*  
788 *the Royal Society of Edinburgh, Section B: Biological Sciences* 96:129–147
- 789 Rasmussen KR, Iversen JD, Rautaheimo P (1996) Saltation and wind flow  
790 interaction in a variable slope wind tunnel. *Geomorphology* 17:19–28
- 791 Raupach M (1992) Drag and drag partition on rough surfaces. *Boundary-Layer*  
792 *Meteorol* 60:375–395
- 793 Rozier O, Narteau C, Gadal C, Claudin P, Courrech du Pont S (2019)  
794 Elongation and stability of a linear dune. *Geophysical Research Letters*  
795 46(24):14521–14530
- 796 Rubin DM, Hunter RE (1987) Bedform alignment in directionally varying  
797 flows. *Science* 237:276–278
- 798 Runyon K, Bridges N, Ayoub F, Newman C, Quade J (2017) An integrated  
799 model for dune morphology and sand fluxes on Mars. *Earth and Planetary*  
800 *Science Letters* 457:204–212
- 801 Sauermann G, Andrade Jr J, Maia L, Costa U, Araújo A, Herrmann H  
802 (2003) Wind velocity and sand transport on a barchan dune. *Geomorphology*  
803 54:245–255
- 804 Seidel DJ, Zhang Y, Beljaars A, Golaz JC, Jacobson AR, Medeiros B (2012)  
805 Climatology of the planetary boundary layer over the continental United  
806 States and Europe. *J Geophys Res* 117:D17106
- 807 Shao Y (2008) Physics and modelling of wind erosion, vol 37. Springer Science  
808 & Business Media
- 809 Shen Y, Zhang C, Huang X, Wang X, Cen S (2019) The effect of wind speed  
810 averaging time on sand transport estimates. *Catena* 175:286–293
- 811 Sheridan PF, Vosper SB (2006) A flow regime diagram for forecasting lee  
812 waves, rotors and downslope winds. *Meteorol Appl* 13:179–195
- 813 Sherman CA (1978) A mass-consistent model for wind fields over complex  
814 terrain. *J Appl Meteorol Clim* 17:312–319
- 815 Sherman D, Farrell E (2008) Aerodynamic roughness lengths over movable  
816 beds: Comparison of wind tunnel and field data. *J Geophys Res* 113:1–10
- 817 Sherman DJ, Li B (2012) Predicting aeolian sand transport rates: A reevalu-  
818 ation of models. *Aeolian Res* 3:371–378
- 819 Smith AB, Jackson DWT, Cooper JAG (2017) Three-dimensional airflow and  
820 sediment transport patterns over barchan dunes. *Geomorphology* 278:28–42

- 821 Song Q, Gao X, Lei J, Li S (2019) Spatial distribution of sand dunes and their  
822 relationship with fluvial systems on the southern margin of the Taklimakan  
823 Desert, China. *Geomatics, Natural Hazards and Risk* 10:2408–2428
- 824 Spalding DB (1961) A single formula for the law of the wall. *Journal of Applied  
Mechanics* 28:455–458
- 825 Stull R (2006) 9 - the atmospheric boundary layer. In: Wallace JM, Hobbs PV  
826 (eds) *Atmospheric Science* (Second Edition), second edition edn, Academic  
827 Press, San Diego, pp 375–417
- 828 Stull RB (1988) An introduction to boundary layer meteorology, vol 13.  
829 Springer Science & Business Media
- 830 Sullivan PP, McWilliams JC (2010) Dynamics of winds and currents coupled  
831 to surface waves. *Annu Rev Fluid Mech* 42:19–42
- 832 Sweet M, Kocurek G (1990) An empirical model of aeolian dune lee-face air-  
833 flow. *Sedimentology* 37:1023–1038
- 834 Sykes RI (1980) An asymptotic theory of incompressible turbulent boundary-  
835 layer flow over a small hump. *J Fluid Mech* 101:647–670
- 836 Taylor P, Teunissen H (1987) The Askervein hill project: overview and back-  
837 ground data. *Boundary-Layer Meteorol* 39:15–39
- 838 Taylor P, Mason P, Bradley E (1987) Boundary-layer flow over low hills.  
839 *Boundary-Layer Meteorol* 39:107–132
- 840 Tsoar H, Yaalon DH (1983) Deflection of sand movement on a sinuous longi-  
841 tudinal (seif) dune: use of fluorescent dye as tracer. *Sedimentary Geology*  
842 36:25–39
- 843 Ungar JE, Haff PK (1987) Steady state saltation in air. *Sedimentology* 34:289–  
844 299
- 845 Unsworth C, Parsons D, Hardy R, Reesink A, Best J, Ashworth P, Keevil G  
846 (2018) The impact of nonequilibrium flow on the structure of turbulence  
847 over river dunes. *Water Resour Res* 54:6566–6584
- 848 Uppala SM, Källberg P, Simmons AJ, Andrae U, Bechtold VDC, Fiorino M,  
849 Gibson J, Haseler J, Hernandez A, Kelly G, et al. (2005) The ERA-40 re-  
850 analysis. *Q J R Meteorol Soc* 131:2961–3012
- 851 Valance A, Rasmussen K, Ould El Moctar A, Dupont P (2015) The physics  
852 of aeolian sand transport. *C R Phys* 16:1–13
- 853 Venditti JG, Best JL, Church M, Hardy RJ (2013) *Coherent Flow Structures  
854 at Earth's Surface*. John Wiley & Sons
- 855 Virtanen P, Gommers R, Oliphant TE, Haberland M, Reddy T, Cournapeau  
856 D, Burovski E, Peterson P, Weckesser W, Bright J, et al. (2020) Scipy 1.0:  
857 fundamental algorithms for scientific computing in python. *Nature methods*  
858 17:261–272
- 859 Vogelezang D, Holtslag A (1996) Evaluation and model impacts of alternative  
860 boundary-layer height formulations. *Boundary-Layer Meteorol* 81:245–269
- 861 Vosper SB (2004) Inversion effects on mountain lee waves. *Q J R Meteorol Soc*  
862 130:1723–1748
- 863 Walker I, Davidson-Arnott R, Bauer B, Hesp P, Delgado-Fernandez I, Oller-  
864 head J, Smyth T (2017) Scale-dependent perspectives on the geomorphology  
865 and evolution of beach-dune systems. *Earth-Science Review* 171:220–253

- 867 Walker IJ, Nickling WG (2002) Dynamics of secondary airflow and sediment  
868 transport over and in the lee of transverse dunes. *Prog Phys Geogr* 26:47–75
- 869 Walker IJ, Hesp PA, Davidson-Arnott RG, Ollerhead J (2006) Topographic  
870 steering of alongshore airflow over a vegetated foredune: Greenwich Dunes,  
871 Prince Edward Island, Canada. *Journal of Coastal Research* 22:1278–1291
- 872 Walker IJ, Hesp PA, Davidson-Arnott RG, Bauer BO, Namikas SL, Ollerhead  
873 J (2009) Responses of three-dimensional flow to variations in the angle of  
874 incident wind and profile form of dunes: Greenwich Dunes, Prince Edward  
875 Island, Canada. *Geomorphology* 105:127–138
- 876 Walmsley JL, Salmon J, Taylor P (1982) On the application of a model of  
877 boundary-layer flow over low hills to real terrain. *Boundary-Layer Meteorol*  
878 23:17–46
- 879 Weaver C, Wiggs G (2011) Field measurements of mean and turbulent airflow  
880 over a barchan sand dune. *Geomorphology* 128:32–41
- 881 Werner BT, Kocurek G (1999) Bedform spacing from defect dynamics. *Geol-*  
882 *ogy* 27:727–730
- 883 Wiggs G, Bullard J, Garvey B, Castro I (2002) Interactions between airflow  
884 and valley topography with implications for aeolian sediment transport.  
885 *Physical Geography* 23:366–380
- 886 Wood N (2000) Wind flow over complex terrain: a historical perspective and  
887 the prospect for large-eddy modelling. *Boundary-Layer Meteorol* 96:11–32
- 888 Zhang C, Li Q, Zhou N, Zhang J, Kang L, Shen Y, Jia W (2016) Field obser-  
889 vations of wind profiles and sand fluxes above the windward slope of a sand  
890 dune before and after the establishment of semi-buried straw checkerboard  
891 barriers. *Aeolian Res* 20:59–70
- 892 Zhang D, Yang X, Rozier O, Narteau C (2014) Mean sediment residence time in  
893 barchan dunes. *Journal of Geophysical Research: Earth Surface* 119(3):451–  
894 463
- 895 Zilker DP, Hanratty TJ (1979) Influence of the amplitude of a solid wavy wall  
896 on a turbulent flow. part 2. separated flows. *J Fluid Mech* 90:257–271
- 897 Zilker DP, Cook GW, Hanratty TJ (1977) Influence of the amplitude of a solid  
898 wavy wall on a turbulent flow. part 1. non-separated flows. *J Fluid Mech*  
899 82:29–51

900           **Local wind regime induced by giant linear dunes**  
 901           — Supplementary Material —

902   **C. Gadal\* · P. Delorme · C. Narteau · G.F.S. Wiggs · M. Baddock ·**  
 903   **J.M. Nield · P. Claudin**

904  
 905   \* Institut de Mécanique des Fluides de Toulouse, Université de Toulouse Paul  
 906   Sabatier, CNRS, Toulouse INP-ENSEEIHT, Toulouse, France.  
 907   cyril.gadal@imft.fr

908   **1. Shear velocity and calibration of the hydrodynamical roughness**

909   As the regionally predicted and locally measured velocities are available at  
 910   different heights, we can not compare them directly. We therefore convert  
 911   all velocities into shear velocities  $u_*$ , characteristic the turbulent logarithmic  
 912   velocity profile (Spalding 1961; Stull 1988):

$$\frac{u(z)}{u_*} = \frac{1}{\kappa} \ln \left( \frac{z}{z_0} \right), \quad (15)$$

913   where  $z$  is the vertical coordinate,  $\kappa = 0.4$  the von Kármán constant and  $z_0$  the  
 914   hydrodynamic roughness. Note that, strickly speaking, this logarithmic profile  
 915   is valid for a neutrally stratified ABL only. Vertical density gradients occurring  
 916   in other conditions may thus induce large discrepancies (Monin and Obukhov  
 917   1954; Garratt 1994; Dyer 1974). However, as our wind measurements are in  
 918   the flow region close enough to the surface, where these effects are negligible,  
 919   this logarithmic wind profile remains a fairly good approximation in all conditions  
 920   (Gunn et al. 2021). Several measurements of hydrodynamic roughnesses  
 921   are available (Raupach 1992; Bauer et al. 1992; Brown et al. 2008; Nield et al.  
 922   2014). In the absence of sediment transport, it is governed by the geometric  
 923   features of the bed (Flack and Schultz 2010; Pelletier and Field 2016). When  
 924   aeolian saltation occurs, it is rather controlled by the altitude of Bagnold's  
 925   focal point (Durán et al. 2011; Valance et al. 2015), which depends on the  
 926   wind velocity and grain properties (Sherman and Farrell 2008; Zhang et al.  
 927   2016; Field and Pelletier 2018). Whether associated with geometric features  
 928   or with sediment transport, its typical order of magnitude is the millimetre  
 929   scale on sandy surfaces.

930   We do not have precise velocity vertical profiles to be able to deduce an  
 931   accurate value of  $z_0$  in the various environments of the meteorological stations  
 932   (vegetated, arid, sandy). Our approach is to rather select the hydrodynamic  
 933   roughness which allows for the best possible matching between the regionally  
 934   predicted and locally measured winds, i.e. minimising the relative difference  $\delta$   
 935   between the wind vectors of both datasets:

$$\delta = \frac{\sqrt{\langle \| \mathbf{u}_{*,\text{era}} - \mathbf{u}_{*,\text{station}} \|^2 \rangle}}{\sqrt{\langle \| \mathbf{u}_{*,\text{era}} \|^2 \rangle \langle \| \mathbf{u}_{*,\text{station}} \|^2 \rangle}}, \quad (16)$$

where  $\langle \cdot \rangle$  denotes time average. This parameter is computed for values of  $z_0$  in ERA5-Land analysis ranging from  $10^{-5}$  m to  $10^{-2}$  m for the four different stations. Note that for the North Sand Sea and South Sand Sea stations, where the giant dunes feedback presumably affect the wind, we take into account the non-deflected winds only in the calculation of  $\delta$  (with a  $15^\circ$  tolerance).

As shown in Online Resource Fig. S3, the minimum values of  $\delta$  in the space  $(z_0^{\text{ERA5Land}}, z_0^{\text{local}})$  form a line. We thus set the roughness in the ERA5-Land analysis to the typical value  $z_0 = 10^{-3}$  m, and deduce the corresponding ones for the local stations. It leads to 2.7, 0.8, 0.1 and 0.5 mm for the Etosha West, North Sand Sea, Huab and South Sand Sea stations, respectively. Importantly, this approach somewhat impacts the calculation of the shear velocities, but not that of the wind directions. As such, most of our conclusions are independent of such a choice. However, it may affect the magnitude of the wind velocity attenuation/amplification in flow confinement situations.

## 2. Computation of the ABL characteristics

The estimation of the non-dimensional numbers associated with the ABL requires the computation of representative meteorological quantities. In arid areas, the vertical structure of the atmosphere can be approximated by a well mixed convective boundary layer of height  $H$ , topped by the stratified free atmosphere (Stull 1988; Shao 2008). In this context, one usually introduces the virtual potential temperature  $T_{\text{vp}}$ , which is a constant  $T_0$  inside the boundary layer, and increases linearly in the FA (Online Resource Fig. S8a):

$$T_{\text{vp}}(z) = \begin{cases} T_0 & \text{for } z \leq H, \\ T_0 \left( 1 + \frac{\Delta T_{\text{vp}}}{T_0} + \frac{N^2}{g}(z - H) \right) & \text{for } z \geq H, \end{cases} \quad (17)$$

where  $\Delta T_{\text{vp}}$  is the temperature discontinuity at the capping layer and  $N = \sqrt{g\partial_z T_{\text{vp}}/T_0}$  is the Brunt-Väisälä frequency, characteristic of the stratification. Note that, under the usual Boussinesq approximation, temperature and air density variations are simply related by  $\delta T_{\text{vp}}/T_0 \simeq -\delta\rho/\rho_0$  (see Online Resource of Andreotti et al. (2009)), so that  $N$  can equivalently be defined from the density gradient as next to (1).

The ERA5 dataset provides vertical profiles of the geopotential  $\phi$ , the actual temperature  $T$  and the specific humidity  $\eta$  at given pressure levels  $P$ . The vertical coordinate is then calculated as:

$$z = \frac{\phi R_t}{g R_t - \phi}, \quad (18)$$

where  $R_t = 6371229$  m is the reference Earth radius and  $g = 9.81$  m s $^{-2}$  is the gravitational acceleration. One also computes the virtual potential temperature as:

$$T_{\text{vp}} = T \left[ 1 + \left( \frac{M_d}{M_w} - 1 \right) \eta \right] \left( \frac{P_0}{P} \right)^{R/C_p}, \quad (19)$$

where  $P_0 = 10^5$  Pa is the standard pressure,  $R = 8.31$  J/K is the ideal gas constant,  $C_p \simeq 29.1$  J/K is the air molar heat capacity, and  $M_w = 0.018$  kg/Mol and  $M_d = 0.029$  kg/Mol are the molecular masses of water and dry air respectively. The specific humidity is related to the vapour pressure  $p_w$  as

$$\eta = \frac{\frac{M_w}{M_d} p_w}{p - \left(1 - \frac{M_w}{M_d}\right) p_w}. \quad (20)$$

The ERA5 dataset also provides an estimate of the ABL depth  $H$ , based on the behaviour of the Richardson vertical profile. This dimensionless number is defined as the ratio of buoyancy and flow shear terms, and can be expressed as  $\text{Ri} = N^2 / (\partial_z u)^2$ . It vanishes in the lower well-mixed layer where  $T_{\text{vp}}$  is constant, and increases in the stratified FA. Following the method and calibration of Vogezezang and Holtlag (1996); Seidel et al. (2012), the value  $\text{Ri}(z) \simeq 0.25$  has been shown to be a good empirical criterion to give  $z \simeq H$  within a precision varying from 50% for the shallower ABL (e.g. at night) to 20% for situations of stronger convection.

Examples of vertical virtual potential temperature profiles deduced from ERA5 are shown in Online Resource Fig. S8a. For each of them, an average temperature is computed below the ABL depth ( $z < H$ ), and a linear function is fitted above, allowing us to extract the temperature jump  $\Delta T_{\text{vp}}$ . Importantly, some profiles display a vertical structure that cannot be approximated by the simple form (17) used here (Online Resource Fig. S8b). In practice, we removed from the analysis all of those leading to the unphysical case  $\Delta T_{\text{vp}} < 0$ . We have noticed that these ‘ill-processed’ profiles dominantly occur in winter and are evenly spread across the hours of the day. Importantly, they represent  $\simeq 12\%$  of the data only (Online Resource Fig. S8c,d), and we are thus confident that this data treatment does not affect our conclusions.

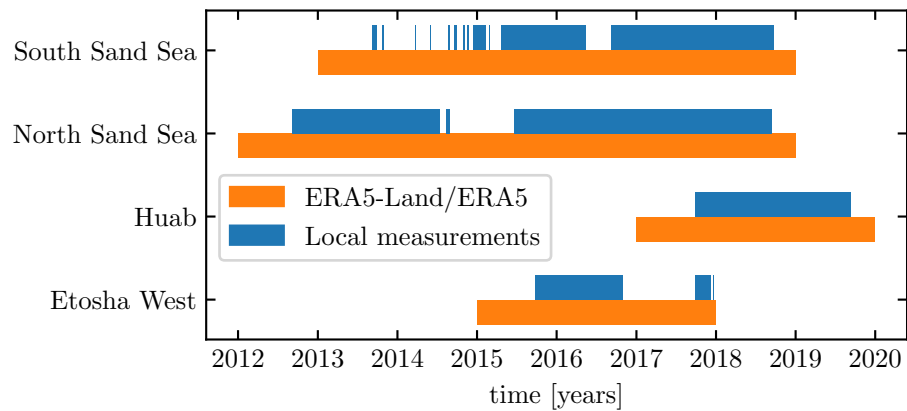


**Fig. S1** Gantt chart representing the valid time steps for the two data sets, for all stations.

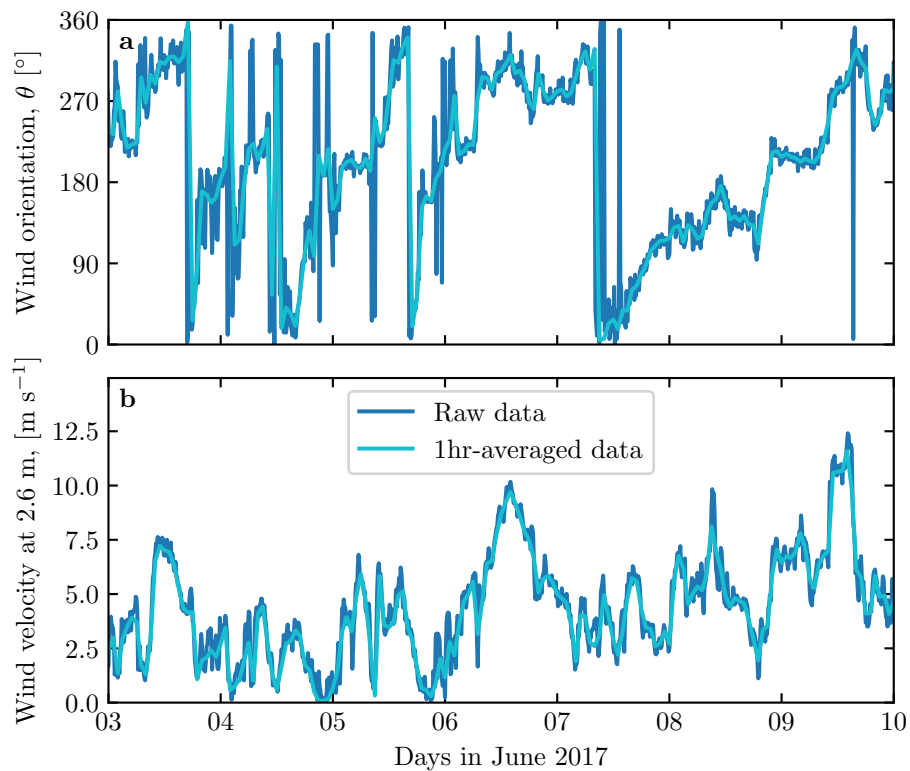


**Fig. S2** Local wind measurements: comparison between raw (blue) and hourly-averaged (light blue) data from South Sand Sea station. **a:** wind direction. **b:** wind velocity at height 2.6 m.

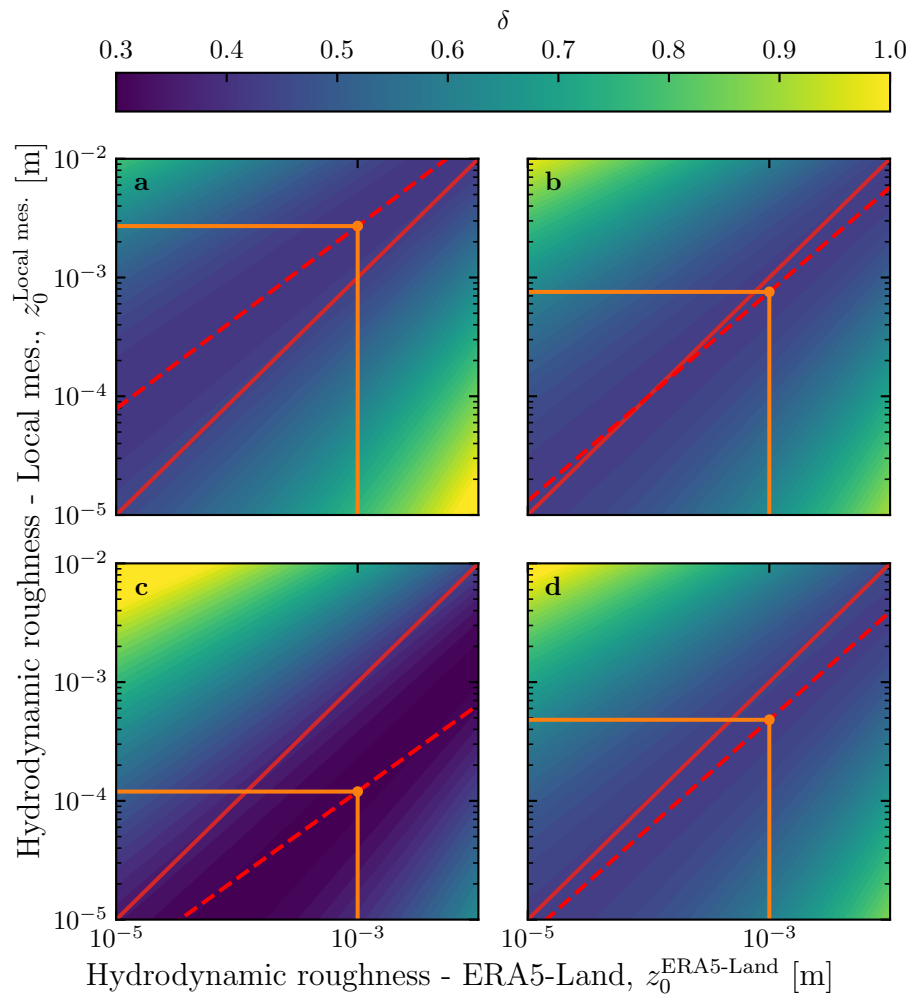


**Fig. S3** Calibration of hydrodynamic roughness. The parameter  $\delta$  (16) quantifying the difference between local and predicted winds is shown in color scale as a function of the hydrodynamic roughnesses chosen for the ERA5-Land and for local winds, for the (a) Etosha West, (b) North Sand Sea, (c) Huab and (d) South Sand Sea stations. The red dashed and plain lines shows the minima of  $\delta$  and the identity line, respectively. The orange lines and dots highlight the chosen hydrodynamic roughnesses for the local winds deduced from setting  $z_0^{\text{ERA5-Land}} = 1 \text{ mm}$ .

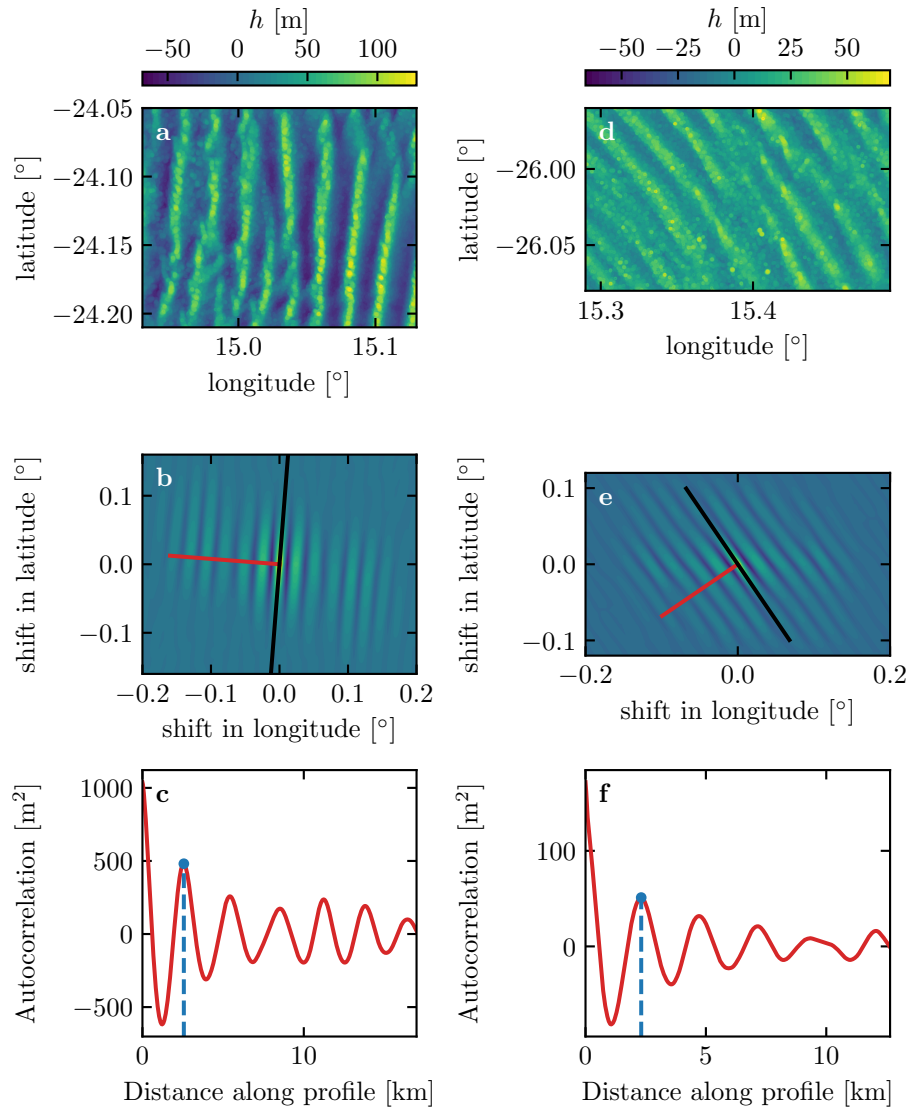


**Fig. S4** Analysis of the DEMs of the North Sand Sea (left column – panels **a**, **b**, **c**) and South Sand Sea (right column – panels **d**, **e**, **f**) stations. **a–d**: Bed elevation detrended by a fitted second order polynomial base-line. **b–e**: Autocorrelation matrix shown in color scale. The black line shows the detected dune orientation, and the red line represents the autocorrelation profile along which the dune wavelength is calculated, displayed in **c–f**. The blue lines and dots show the first peak of the autocorrelation profile, whose abscissa gives the characteristic wavelength of the dune pattern.

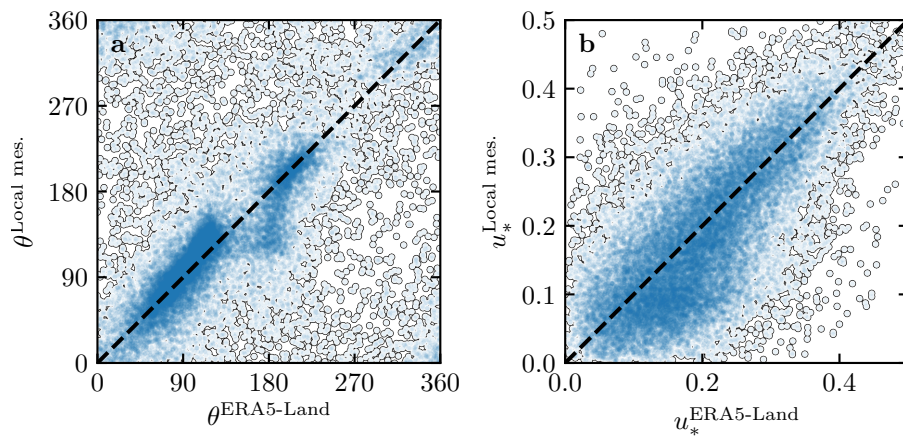


**Fig. S5** Statistical comparison of the wind orientation (a) and velocity (b) between the ERA5-Land dataset and the local measurements for the Huab and Etosha West stations. Data point clustering around identity lines (dashed and black) provide evidence for agreement of the two sets.

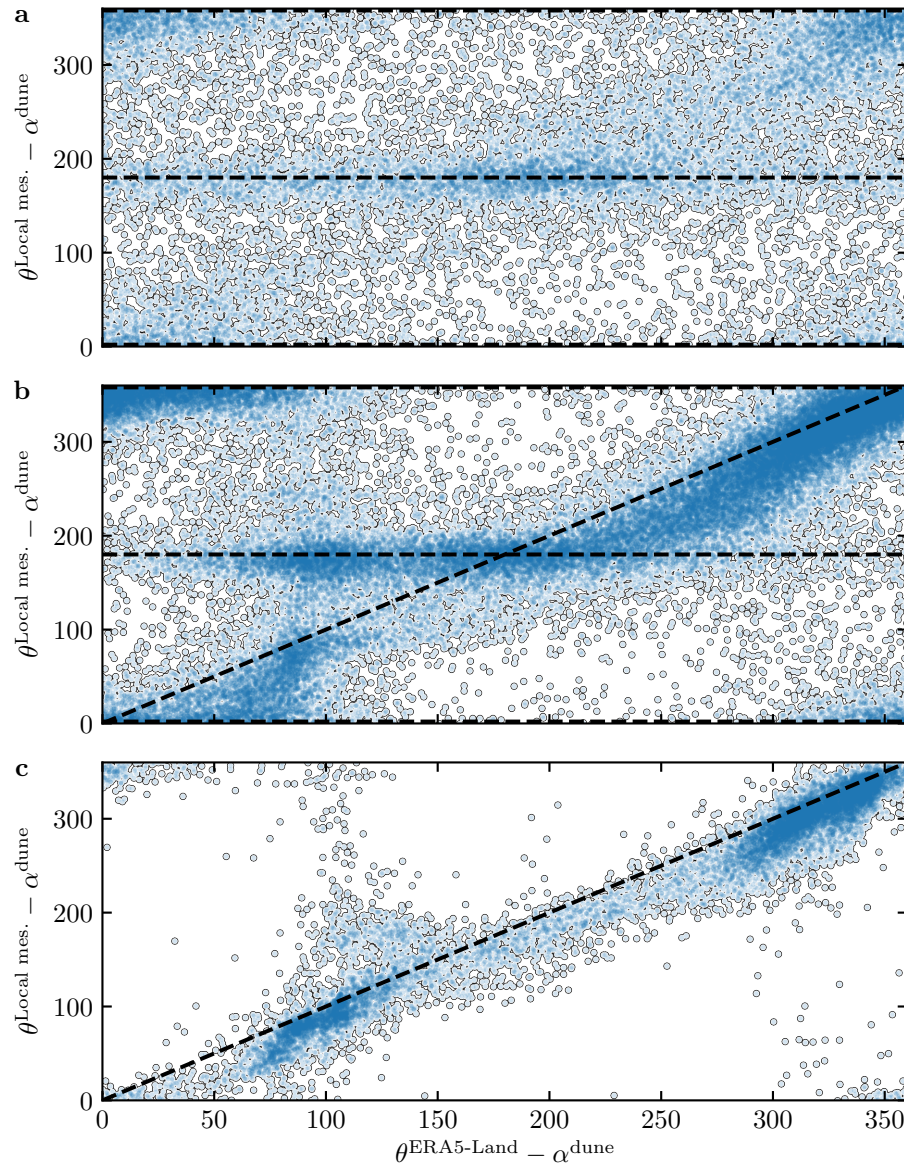


**Fig. S6** Statistical comparison of the wind orientation between the ERA5-Land dataset and the local measurements for the South Sand Sea and North Sand Sea stations, for different velocity ranges. **a:**  $u_*^{\text{ERA5-Land}} < 0.1 \text{ m s}^{-1}$ . **b:**  $0.1 < u_*^{\text{ERA5-Land}} \leq 0.25 \text{ m s}^{-1}$ . **c:**  $u_*^{\text{ERA5-Land}} \geq 0.25 \text{ m s}^{-1}$ . The measured dune orientations are subtracted to the wind orientation, which allows us to plot both stations on the same graph. Black dashed lines indicate locally measured orientations aligned with the dune crests (here 0°, 180° and 360° – panels **a**, **b**), as well as the identity lines (panels **b**, **c**).

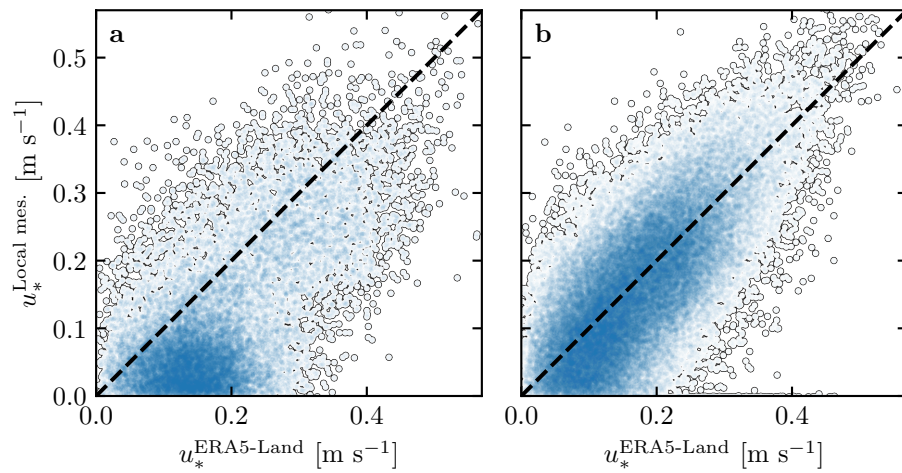


**Fig. S7** Statistical comparison of the wind velocity between the ERA5-Land dataset and the local measurements for the South Sand Sea and North Sand Sea stations. **a:** Nocturnal summer easterly wind. **b:** Diurnal southerly wind. Black dashed lines are identity lines. The angle ranges used to select diurnal and nocturnal summer winds are the same as those in Figs. 4 and Figs. 6 of the main article.

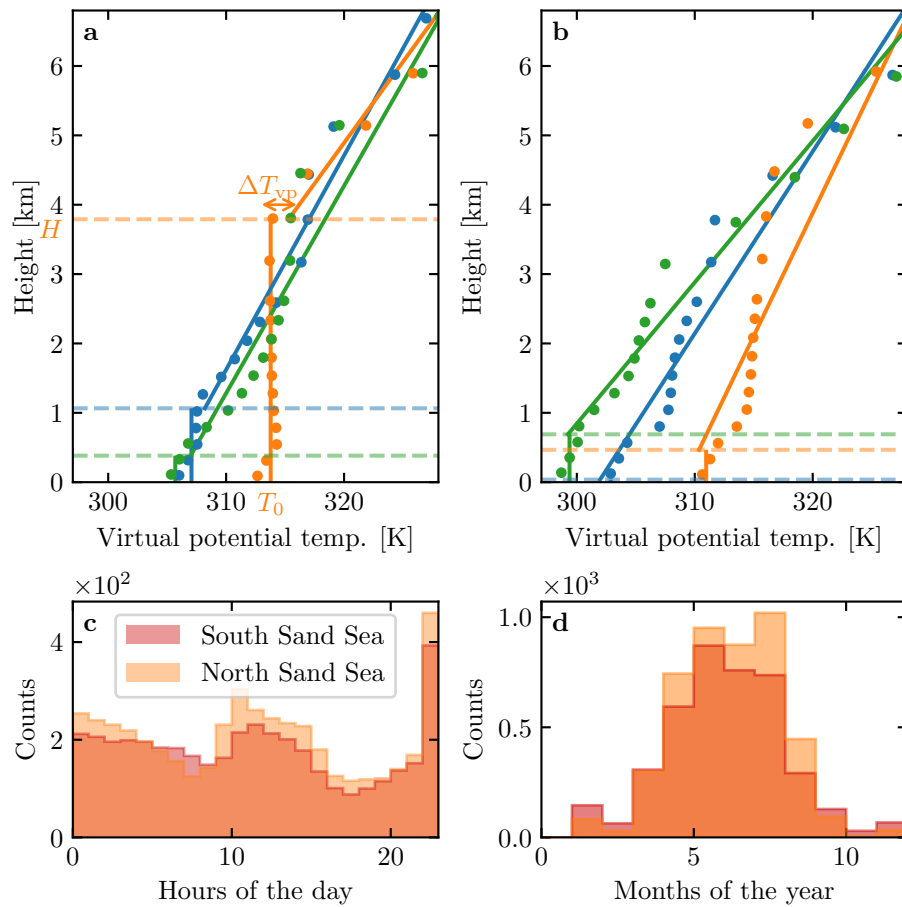


**Fig. S8** **a:** Vertical profiles of the virtual potential temperature at three different times (blue: 29/11/2012 - 11.00 UTC, orange: 21/03/2017 - 12.00 UTC, green: 21/03/2017 - 20.00 UTC) at the South Sand Sea station. Dots: data from the ERA5 reanalysis. Dashed lines: boundary layer height given by the ERA5 reanalysis. Plain lines: vertical (ABL) and linear (FA) fits to estimate the quantities displayed in Online Resource Fig. S9. **b:** Examples of ill-processed vertical profiles at three different times (blue: 2/12/2013 - 23.00 UTC, orange: 20/03/2017 - 00.00 UTC, green: 14/07/2017 - 14.00 UTC) at the South Sand Sea station. Distribution of ill-processed vertical profiles at South (orange) and North (light orange) Sand Sea station: hourly **(c)** and monthly **(d)** counts.

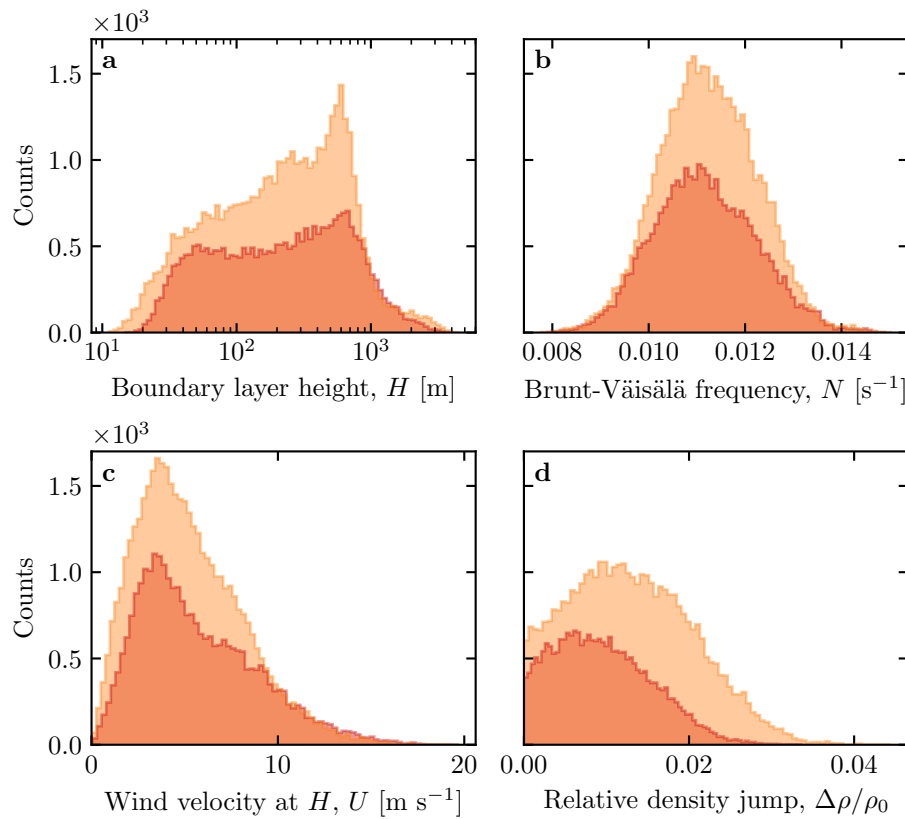


**Fig. S9** Distributions of the meteorological parameters resulting from the processing of the ERA5-Land data for the South Sand Sea (orange) and the North Sand Sea (light orange) stations.

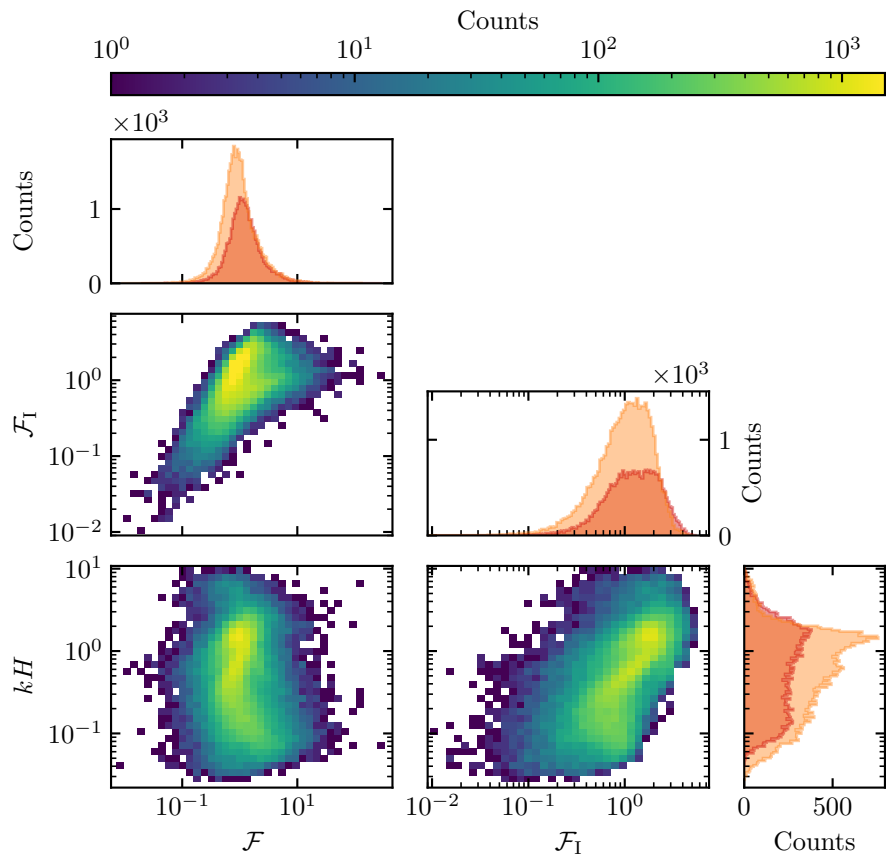


**Fig. S10** Non-dimensional parameters distributions. For the marginal distributions, the light orange corresponds to the South Sand Sea station, and the orange to the North Sand Sea station.

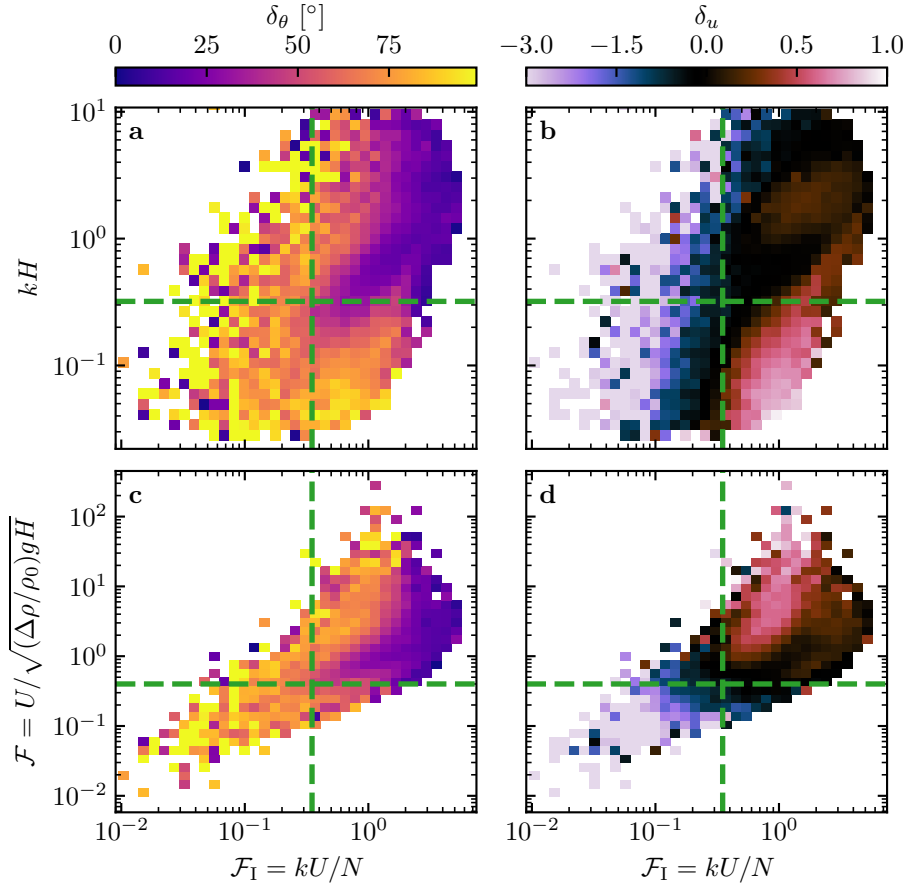


**Fig. S11** Regime diagrams of the wind deviation  $\delta_\theta$  and relative attenuation/amplification  $\delta_u$  in the spaces  $(\mathcal{F}_I, kH)$  and  $(\mathcal{F}_I, \mathcal{F})$ , containing the data from both the North Sand Sea and South Sand Sea stations. Green dashed lines empirically delimit the different regimes. The point density in each bin of the diagrams is shown in Online Resource Fig. S10 – 95% of the data occur in the range  $-1 < \delta u < 1$ . The similar regime diagrams in the space  $(\mathcal{F}, kH)$  are shown in Fig. 8.

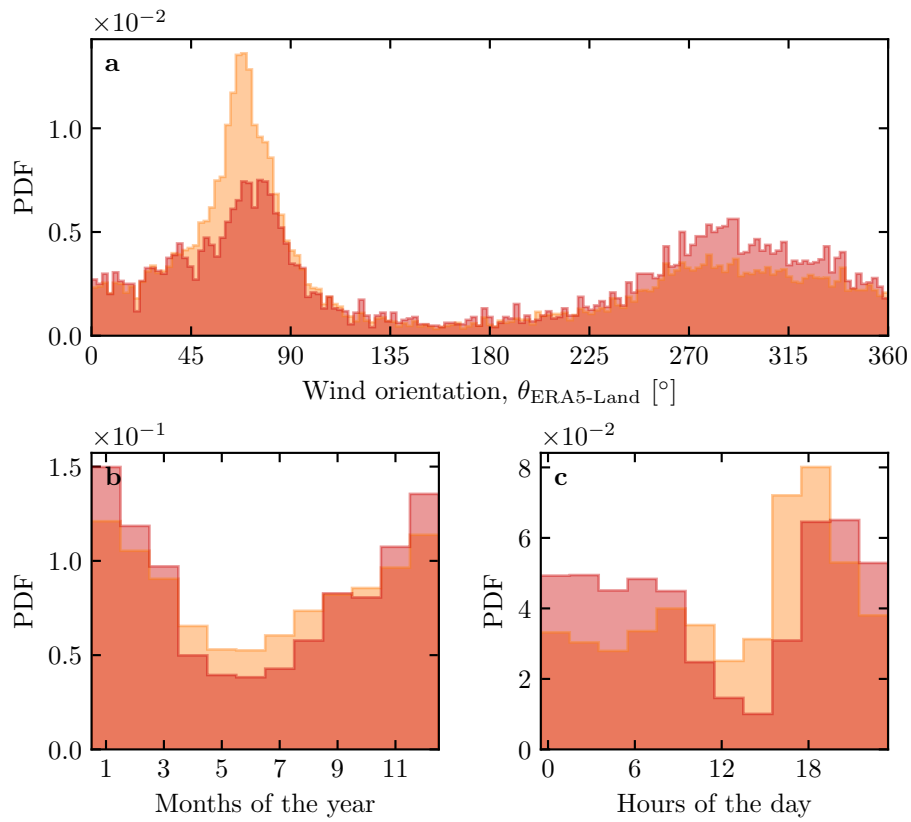


**Fig. S12** Normalized distributions of amplified velocities for the North Sea (light orange:  $\delta_u < 0$ , orange:  $\delta_u < -0.5$ ). **a:** Angular distributions. **b:** Monthly distributions. **c:** Hourly distributions.

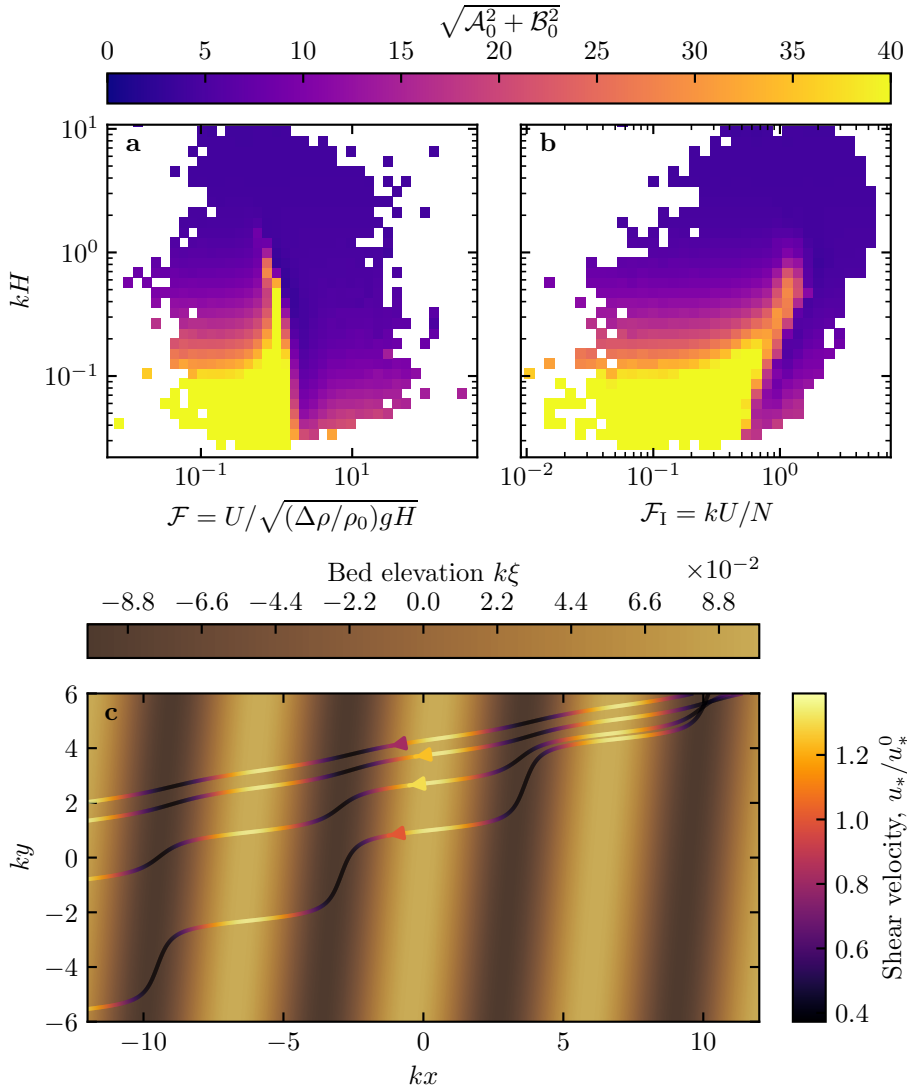


**Fig. S13** Computation of the flow disturbance with the linear model of Andreotti et al. (2009). **a–b:** Magnitude of the hydrodynamic coefficients  $A_0$  and  $B_0$ , calculated from the time series of the non-dimensional numbers corresponding to the ERA5-Land wind data and ERA5 data on vertical pressure levels. **c** Shear velocity streamlines over sinusoidal ridges of amplitude  $k\xi_0 = 0.1$  and for increasing values of  $\sqrt{A_0^2 + B_0^2}$ . From the upper to the lower streamline, values of  $(kH, \mathcal{F}, \mathcal{F}_I, A_0, B_0, \sqrt{A_0^2 + B_0^2})$  are  $(1.9, 0.6, 1.5, 3.4, 1.0, 3.5)$ ,  $(1.5, 0.3, 0.4, 4.8, 1.4, 5.0)$ ,  $(0.1, 3.5, 1.0, 8.6, 0.1, 8.6)$ ,  $(0.5, 0.05, 0.04, 9.6, 2.5, 9.9)$ .

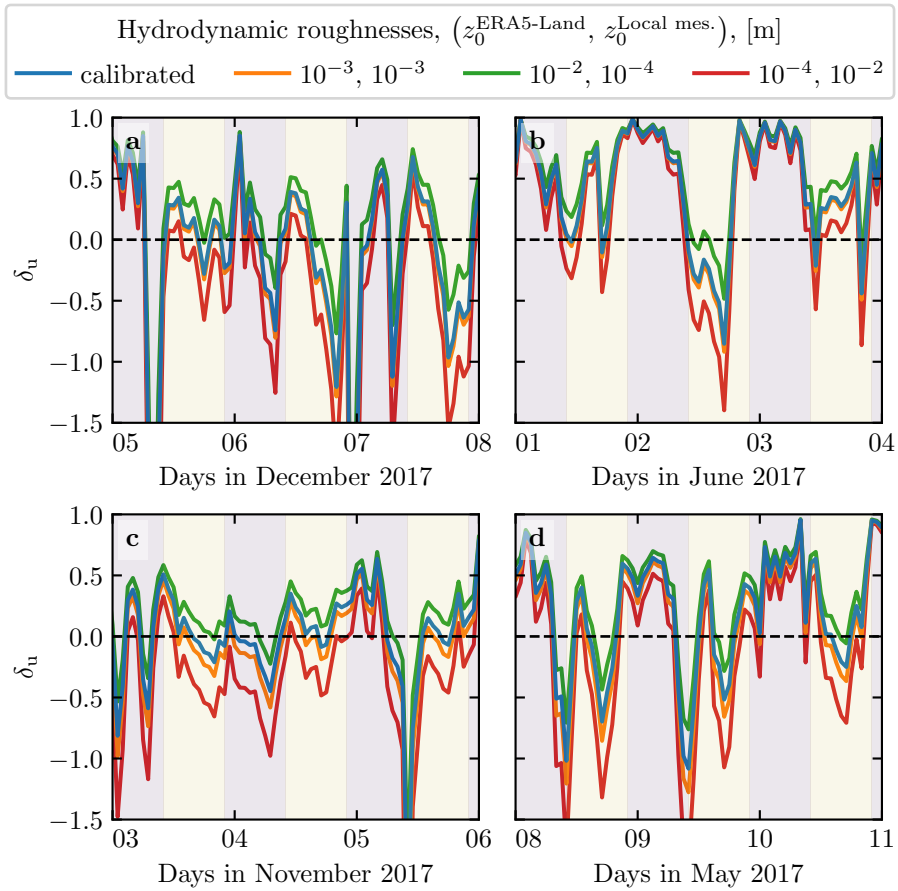


**Fig. S14** Time series of the relative velocity disturbance  $\delta_u$  corresponding to Fig. 5, for different values of the hydrodynamic roughnesses. **a:** North Sand Sea – summer, **b:** North Sand Sea – winter, **d:** South Sand Sea – summer, **e:** South Sand Sea – winter. Note that  $\delta_\theta$  is independent of the choice of  $z_0^{\text{ERA5-Land}}$  and  $z_0^{\text{Local mes.}}$ .